Spectroscopic Properties and Electronic Structure of Low-Spin Fe(III)−Alkylperoxo Complexes: Homolytic Cleavage of the O−O Bond

Nicolai Lehnert,[†] Raymond Y. N. Ho,[‡] Lawrence Que, Jr.,*[,‡] and Edward I. Solomon*[,†]

Contribution from the Department of Chemistry, Stanford University, Stanford, California 94305-5080, and Department of Chemistry and Center for Metals in Biocatalysis, University of Minnesota, Minneapolis, Minnesota 55455

Received January 19, 2001. Revised Manuscript Received May 8, 2001

Abstract: The spectroscopic properties, electronic structure, and reactivity of the low-spin Fe(III)−alkylperoxo model complex $[Fe(TPA)(OH_x)(OO^tBu)]^{x+}$ (**1**; TPA = tris(2-pyridylmethyl)amine, ^tBu = *tert*-butyl, $x = 1$ or 2) are explored. The vibrational spectra of **1** show three peaks that are assigned to the O−O stretch (796 cm^{-1}), the Fe−O stretch (696 cm^{-1}), and a combined O−C−C/C−C−C bending mode (490 cm^{-1}) that is mixed with ν(FeO). The corresponding force constants have been determined to be 2.92 mdyn/Å for the O−O bond which is small and 3.53 mdyn/Å for the Fe−O bond which is large. Complex **1** is characterized by a broad absorption band around 600 nm that is assigned to a charge-transfer (CT) transition from the alkylperoxo π^*_ν to a t_{2g} d orbital of Fe(III). This metal−ligand π bond is probed by MCD and resonance Raman spectroscopies which show that the CT state is mixed with a ligand field state ($t_{2g} \rightarrow e_g$) by configuration interaction. This gives rise to two intense transitions under the broad 600 nm envelope with CT character which are manifested by a pseudo-**A** term in the MCD spectrum and by the shapes of the resonance Raman profiles of the 796, 696, and 490 cm^{-1} vibrations. Additional contributions to the Fe−O bond arise from σ interactions between mainly O−O bonding donor orbitals of the alkylperoxo ligand and an e_g d orbital of Fe(III), which explains the observed O−O and Fe−O force constants. The observed homolytic cleavage of the O−O bond of **1** is explored with experimentally calibrated density functional (DFT) calculations. The O−O bond homolysis is found to be endothermic by only 15 to 20 kcal/mol due to the fact that the Fe(IV)═O species formed is highly stabilized (for spin states $S = 1$ and 2) by two strong π and a strong σ bond between Fe(IV) and the oxo ligand. This low endothermicity is compensated by the entropy gain upon splitting the O−O bond. In comparison, Cu(II)−alkylperoxo complexes studied before [Chen, P.; Fujisawa, K.; Solomon, E. I. *J. Am. Chem. Soc.* **2000**, *122*, 10177] are much less suited for O−O bond homolysis, because the resulting Cu(III)═O species is less stable. This difference in metal−oxo intermediate stability enables the O−O homolysis in the case of iron but directs the copper complex toward alternative reaction channels.

Introduction

Mononuclear non-heme iron enzymes are involved in many different types of oxidation reactions of substrates including hydroxylation and hydroperoxidation of C−H bonds, cleavage of aromatic rings, and oxidative ring closure. The anti-cancer drug bleomycin (BLM), which has a non-heme like coordination sphere of iron, catalyzes H-atom abstraction from the C_4' position of DNA ribose sugar.[1] Many of these reactions are believed to proceed via Fe(III)−alkylperoxo or −hydroperoxo intermediates.[2] For the cofactor-dependent hydroxylases (for example, phenylalanine hydroxylase or clavaminate synthase), Fe(III)−OOR species are possible reaction intermediates where R is the organic cofactor (pterin or α-ketoglutarate). The hydroxylation reactions performed by Rieske-type dioxygenases, on the other hand, are thought to involve Fe(III)−OOH or side-on Fe(III)−peroxo reactive species. However, for the non-heme iron enzymes no reaction intermediate has yet been characterized. In the case of Lipoxygenase, a stable high-spin Fe(III)−alkylperoxo complex is formed either as an enzyme−product complex or in a side reaction.[2−6] The only peroxo-level intermediate that has been studied in the field of non-heme iron is activated bleomycin (ABLM), which is a low-spin Fe(III)−OOH complex.[7−13]

[†] Stanford University.

[‡] University of Minnesota.

(1) Holm, R. H.; Kennepohl, P.; Solomon, E. I. *Chem. Rev.* **1996**, *96*, 2239−2314.

(2) (a) Solomon, E. I.; Brunold, T. C.; Davis, M. I.; Kemsley, J. N.; Lee, S.-K.; Lehnert, N.; Neese, F.; Skulan, A. J.; Yang, Y.-S.; Zhou, J. *Chem. Rev.* **2000**, *100*, 235−349. (b) Que, L., Jr.; Ho, R. Y. N. *Chem. Rev.* **1996**, *96*, 2607−2624.

(3) De Groot, J. J. M. C.; Garssen, G. J.; Veldink, G. A.; Vliegenthart, J. F. G.; Boldingh, J. *FEBS Lett.* **1975**, *56*, 50−54.

(4) Spaapen, L. J. M.; Veldink, G. A.; Liefkens, T. J.; Vliegenthart, J. F. G.; Kay, C. M. *Biochim. Biophys. Acta* **1979**, *574*, 301−311.

(5) Slappendel, S.; Veldink, G. A.; Vliegenthart, J. F. G.; Aasa, R.; Malmström, B. G. *Biochim. Biophys. Acta* **1983**, *747*, 32−36.

(6) Nelson, M. J.; Chase, D. B.; Seitz, S. P. *Biochemistry* **1995**, *34*, 6159−6163.

(7) Burger, R. M.; Peisach, J.; Horwitz, S. B. *J. Biol. Chem.* **1981**, *256*, 11636−11644.

(8) Burger, R. M.; Kent, T. A.; Horwitz, S. B.; Münck, E.; Peisach, J. *J. Biol. Chem.* **1983**, *258*, 1559−1564.

(9) Sam, J. W.; Tang, X.-J.; Peisach, J. *J. Am. Chem. Soc.* **1994**, *116*, 5250−5256.

(10) Takahashi, S.; Sam, J. W.; Peisach, J.; Rousseau, D. L. *J. Am. Chem. Soc.* **1994**, *116*, 4408−4413.

(11) Veselov, A.; Sun, H.; Sienkiewicz, A.; Taylor, H.; Burger, R. M.; Scholes, C. P. *J. Am. Chem. Soc.* **1995**, *117*, 7508−7512.

10.1021/ja010165n CCC: $20.00
Published on Web 08/04/2001

Three different mechanisms have been discussed for the H-atom abstraction reaction of ABLM: (a) heterolytic cleavage of the O−O bond generating a catalytically active formally Fe(V)═O species; (b) homolytic cleavage leading to a reactive Fe(IV)═O intermediate; or (c) direct H-atom abstraction by the hydroperoxo complex. The formally Fe(V)═O species formed by heterolytic cleavage (a) of the O−O bond of the protonated hydroperoxo ligand has been observed in heme systems.[14−19] This intermediate is stabilized by oxidation of the porphyrin ligand (P) leading to a ($P^{+\bullet}$)Fe(IV)═O species ("compound I"),[20−25] which is catalytically active in H-atom abstraction. Heterolytic cleavage of the O−O bond has been shown by DFT calculations to be highly favorable for porphyrin systems with a reaction energy of about −80 kcal/mol.[13,26] However, the BLM ligand is much harder to oxidize compared to a porphyrin, hence it is much less suited to stabilize a high-valent Fe(V)═O species. Correspondingly, the O−O bond heterolysis for ABLM has been calculated to be endothermic by ∼80 kcal/mol with DFT and, therefore, highly unfavorable.[13] Homolotic cleavage (b) of the O−O bond, which leads to the generation of a free •OH radical along with an Fe(IV)═O species, has been ruled out for ABLM based on the high specificity of the reaction of ABLM with DNA.[27−29] On the basis of these results, the direct reaction (c) of ABLM with the C−H bond of the DNA sugar to abstract an H-atom has been proposed.[13] This reaction has been calculated with DFT to be close to thermoneutral. Here, the empty σ^* orbital of the hydroperoxo ligand is low in energy and causes the peroxide to be electrophilic. Attack of the C−H bond by σ^* could then lead to a (BLM)Fe(IV)═O intermediate, a water molecule, and the DNA radical.

While no other peroxo level intermediate of a non-heme iron biological system has been spectroscopically characterized besides ABLM, a number of Fe(III)−alkylperoxo and −hydroperoxo model complexes have been synthesized. For several corresponding low-spin complexes, the reactivity toward C−H bonds and olefins has been studied.[2a] Six-coordinate *tert*-butylperoxo complexes have been synthesized for TPA (tris-(2-pyridylmethyl)amine) and other ligand systems.[30−33] Using the unsubstituted TPA ligand, low-spin [Fe(TPA)(OH_x)(OO^tBu)]$^{x+}$ (**1**, $x = 1$ or 2) was obtained and spectroscopically studied. This compound is characterized by an intense absorption at 600 nm, Raman features at 796, 696, and 490 cm^{-1}, and *g*-values of 2.19, 2.14, and 1.98 from EPR spectroscopy.[30,32] In addition, **1** has been characterized by electrospray ionization mass spectrometry. Importantly, this method does not allow the determination of whether water or hydroxide is bound to iron, hence the sixth ligand of **1** is denoted as (OH_x). In addition, a large number of low-spin Fe(III)−hydroperoxo complexes with N-donor ligand systems have been synthesized as models for ABLM.[31,34−44] None of these iron(III) complexes has been structurally characterized, but crystal structures have been obtained for related Co[45−50] and Cu[51−54] systems. Detailed studies on the reactivity of complex **1** with alkanes yielding alcohols and ketones have shown that **1** undergoes homolytic cleavage of the O−O bond:[55−59]

(12) Westre, T. E.; Loeb, K. E.; Zaleski, J. M.; Hedman, B.; Hodgson, K. O.; Solomon, E. I. *J. Am. Chem. Soc.* **1995**, *117*, 1309−1313.

(13) Neese, F.; Zaleski, J. M.; Loeb-Zaleski, K.; Solomon, E. I. *J. Am. Chem. Soc.* **2000**, *122*, 11703−11724.

(14) Groves, J. T. *J. Chem. Educ.* **1985**, *62*, 928−931.

(15) Ortiz de Montellano, P. R. *Cytochrome P450: Structure, Mechanism and Biochemistry*; Plenum: New York, 1985.

(16) Dawson, J. H. *Science* **1988**, *240*, 433−439.

(17) Traylor, T. G.; Traylor, P. S. *Active Oxygen in Chemistry and Biology*; Blackie Academic and Professional: New York, 1995; p 84.

(18) Sono, M.; Roach, M. P.; Coulter, E. D.; Dawson, J. H. *Chem. Rev.* **1996**, *96*, 2841−2887.

(19) Schlichting, I.; Berendzen, J.; Chu, K.; Stock, A. M.; Maves, S. A.; Benson, D. E.; Sweet, R. M.; Ringe, D.; Petsko, G. A.; Sligar, S. G. *Science* **2000**, *287*, 1615.

(20) Moss, T. H.; Ehrenberg, A.; Bearden, A. J. *Biochemistry* **1969**, *8*, 4159−4162.

(21) Schulz, C. E.; Devaney, P. W.; Winkler, H.; Debrunner, P. G.; Doan, N.; Chiang, R.; Rutter, R.; Hager, L. P. *FEBS Lett.* **1979**, *103*, 102−105.

(22) Penner-Hahn, J. E.; McMurry, T. J.; Renner, M.; Latos-Grazynsky, L.; Smith Eble, K.; Davis, I. M.; Balch, A. L.; Groves, J. T.; Dawson, J. H.; Hodgson, K. O. *J. Biol. Chem.* **1983**, *258*, 12761−12764.

(23) Penner-Hahn, J. E.; Smith Eble, K.; McMurry, T. J.; Renner, M.; Balch, A. L.; Groves, J. T.; Dawson, J. H.; Hodgson, K. O. *J. Am. Chem. Soc.* **1986**, *108*, 7819−7825.

(24) Proniewicz, L. M.; Paeng, I. R.; Nakamoto, K. *J. Am. Chem. Soc.* **1991**, *113*, 3294−3303.

(25) Nakamoto, K. *J. Mol. Struct.* **1997**, *408*, 11−16.

(26) Harris, D. L.; Loew, G. H. *J. Am. Chem. Soc.* **1998**, *120*, 8941−8948.

(27) Stubbe, J.; Kozarich, J. W. *Chem. Rev.* **1987**, *87*, 1107−1136.

(28) Stubbe, J.; Kozarich, J. W.; Wu, W.; Vanderwall, D. E. *Acc. Chem. Res.* **1996**, *29*, 322−330.

(29) Burger, R. M. *Chem. Rev.* **1998**, *98*, 1153−1169.

(30) Kim, J.; Larka, E.; Wilkinson, E. C.; Que, L., Jr. *Angew. Chem., Int. Ed. Engl.* **1995**, *34*, 2048−2051.

(31) Nguyen, C.; Guajardo, R. J.; Mascharak, P. K. *Inorg. Chem.* **1996**, *35*, 6273−6281.

(32) Zang, Y.; Kim, J.; Dong, Y.; Wilkinson, E. C.; Appelman, E. H.; Que, L., Jr. *J. Am. Chem. Soc.* **1997**, *119*, 4197−4205.

(33) Wada, A.; Ogo, S.; Watanabe, Y.; Mukai, M.; Kitagawa, T.; Jitsukawa, K.; Masuda, H.; Einaga, H. *Inorg. Chem.* **1999**, *38*, 3592−3593.

(34) Guajardo, R. J.; Hudson, S. E.; Brown, S. J.; Mascharak, P. K. *J. Am. Chem. Soc.* **1993**, *115*, 7971−7977.

(35) Bernal, I.; Jensen, I. M.; Jensen, K. B.; McKenzie, C. J.; Toftlund, H.; Tuchagues, J.-P. *J. Chem. Soc., Dalton Trans.* **1995**, 3667−3675.

(36) Lubben, M.; Meetsma, A.; Wilkinson, E. C.; Feringa, B.; Que, L., Jr. *Angew. Chem., Int. Ed. Engl.* **1995**, *34*, 1512−1514.

(37) de Vries, M. E.; La Crois, R. M.; Roelfes, G.; Kooijman, H.; Spek, A. L.; Hage, R.; Feringa, B. L. *Chem. Commun.* **1997**, 1549−1550.

(38) Kim, C.; Chen, K.; Kim, J.; Que, L., Jr. *J. Am. Chem. Soc.* **1997**, *119*, 5964−5965.

(39) Ho, R. Y. N.; Roelfes, G.; Feringa, B. L.; Que, L., Jr. *J. Am. Chem. Soc.* **1999**, *121*, 264−265.

(40) Chen, K.; Que, L., Jr. *Chem. Commun.* **1999**, 1375−1376.

(41) Lippai, I.; Magliozzo, R. S.; Peisach, J. *J. Am. Chem. Soc.* **1999**, *121*, 780−784.

(42) Roelfes, G.; Lubben, M.; Chen, K.; Ho, R. Y. N.; Meetsma, A.; Genseberger, S.; Hermant, R. M.; Hage, R.; Mandal, S. K.; Young, V. G., Jr.; Zang, Y.; Kooijman, H.; Spek, A. L.; Que, L., Jr.; Feringa, B. L. *Inorg. Chem.* **1999**, *38*, 1929−1936.

(43) Simaan, A. J.; Banse, F.; Mialane, P.; Boussac, A.; Un, S.; Kargar-Grisel, T.; Bouchoux, G.; Girerd, J.-J. *Eur. J. Inorg. Chem.* **1999**, 993−996.

(44) Roelfes, G.; Lubben, M.; Hage, R.; Que, L., Jr.; Feringa, B. L. *Chem. Eur. J.* **2000**, *6*, 2152−2159.

(45) Chiaroni, A.; Pascard-Billy, C. *Bull. Soc. Chim. Fr.* **1973**, 781−787.

(46) Alcock, N. W.; Golding, B. T.; Mwesigye-Kibende, S. *J. Chem. Soc., Dalton Trans.* **1985**, 1997−2000.

(47) Mikolaiski, W.; Baum, G.; Massa, W.; Hoffmann, R. W. *J. Organomet. Chem.* **1989**, *376*, 397−405.

(48) Chavez, F. A.; Nguyen, C. V.; Olmstead, M. M.; Mascharak, P. K. *Inorg. Chem.* **1996**, *35*, 6282−6291.

(49) Chavez, F. A.; Rowland, J. M.; Olmstead, M. M.; Mascharak, P. K. *J. Am. Chem. Soc.* **1998**, *120*, 9015−9027.

(50) Chavez, F. A.; Briones, J. A.; Olmstead, M. M.; Mascharak, P. K. *Inorg. Chem.* **1999**, *38*, 1603−1608.

(51) Kitajima, N.; Katayama, T.; Fujisawa, K.; Iwata, Y.; Moro-oka, Y. *J. Am. Chem. Soc.* **1993**, *115*, 7872−7873.

(52) Fujisawa, K.; Tanaka, M.; Moro-oka, Y.; Kitajima, N. *J. Am. Chem. Soc.* **1994**, *116*, 12079−12080.

(53) Harata, M.; Jitsukawa, K.; Masuda, H.; Einaga, H. *J. Am. Chem. Soc.* **1994**, *116*, 10817−10818.

(54) Wada, A.; Harata, M.; Hasegawa, K.; Jitsukawa, K.; Masuda, H.; Mukai, M.; Kitagawa, T.; Einaga, H. *Angew. Chem., Int. Ed. Engl.* **1998**, *37*, 798−799.

(55) Kojima, T.; Leising, R. A.; Yan, S.; Que, L., Jr. *J. Am. Chem. Soc.* **1993**, *115*, 11328−11335.

(56) Arends, I. W. C. E.; Ingold, K. U.; Wayner, D. D. M. *J. Am. Chem. Soc.* **1995**, *117*, 4710−4711.

(57) Kim, J.; Harrison, R. G.; Kim, C.; Que, L., Jr. *J. Am. Chem. Soc.* **1996**, *118*, 4373−4379.

(58) MacFaul, P. A.; Arends, I. W. C. E.; Ingold, K. U.; Wayner, D. D. M. *J. Chem. Soc., Perkin Trans. 2* **1997**, 135−145.

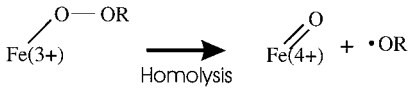

The alkoxy radical •OR is then capable of cleaving C−H bonds by abstracting an H-atom. The resulting C• radical initiates radical chain reactions leading to the observed products. The Fe(IV)═O species may also be capable of H-atom abstraction[44] or insertion of its oxygen atom into a C−H bond.[60] The well-defined reactivity of complex **1** allows us to study the homolytic cleavage of the O−O bond (mechanism (b), vide supra) in relation to the electronic structure of this complex, which is the focus of this paper.

A simplified picture of end-on alkylperoxo binding to Fe(III) has been given.[2a] This description is now extended to the electronic structure of low-spin Fe(III)−alkylperoxo complexes. Figure 1 shows the frontier orbitals of the *tert*-butylperoxo anion with the nomenclature for the different molecular orbitals (MOs). The unoccupied σ^* orbital is at high energy and consists of the antibonding combination of the two p functions along the O−O bond. The lowest unoccupied molecular orbital (LUMO) is diffuse with some C−H antibonding character and does not participate in bonding to iron. The highest occupied molecular orbital (HOMO) of the *tert*-butylperoxo anion (π^*_v, v = vertical) is the antibonding combination of the two p-functions which are perpendicular to the O−O bond *and* to the O−O−C_{3t} plane. Note that π^*_v is a pure oxygen-based MO with no contribution from the carbons. In contrast the π^*_h (h = horizontal) orbital, which is the antibonding combination of p functions perpendicular to the O−O bond and *within* the O−O−C_{3t} plane, is polarized toward the remote oxygen by interaction with a p function of the central carbon. The bonding counterparts of these MOs are found at lower energy in Figure 1. Note that π^b_h and σ^b are close in energy and strongly mixed (both lie within the O−O−C_{3t} plane). When complexed with iron, the *out-of-plane* orbitals π^*_v and π^b_v are oriented to form π bonds with the metal t_{2g} orbitals whereas σ^*, π^*_h, and the mixed π^b_h and σ^b orbitals (all *in-plane*) are potentially involved in σ interactions with the e_g type d functions of the metal. Note that the shapes of the in-plane orbitals change (especially π^b_h and σ^b) upon bonding to iron (vide infra).

In this study we determine the spectroscopic properties of the low-spin (ls) model complex $[Fe(TPA)(OH_x)(OO^tBu)]^{x+}$ (**1**, x = 1 or 2) using resonance Raman, UV−vis, and MCD spectroscopies. Applying normal coordinate analysis (NCA), we derive experimental force constants and fully assign the Raman spectra of **1**. The UV−vis and magnetic circular dichroism (MCD) spectra of **1** are analyzed in relation to the resonance Raman profiles of the assigned vibrations. This enables us to identify a charge-transfer (CT) transition in the UV−vis spectrum which probes one bonding interaction between iron(III) and alkylperoxide. To complete the description of the electronic structure of **1**, density functional (DFT) calculations have been performed on possible structural models of **1**. The DFT results are related to the available experimental data to estimate the geometric and electronic structure of this complex. Finally, we examine the observed reactivity of **1** (vide supra) using the experimentally calibrated DFT calculations and evaluate the electronic structure of the putative Fe(IV)═O intermediate which results from the homolytic cleavage of the O−O bond. A comparison of Fe(IV)═O to Cu(III)═O provides insight into why homolytic cleavage is more favored for the non-heme iron systems compared to Cu complexes.

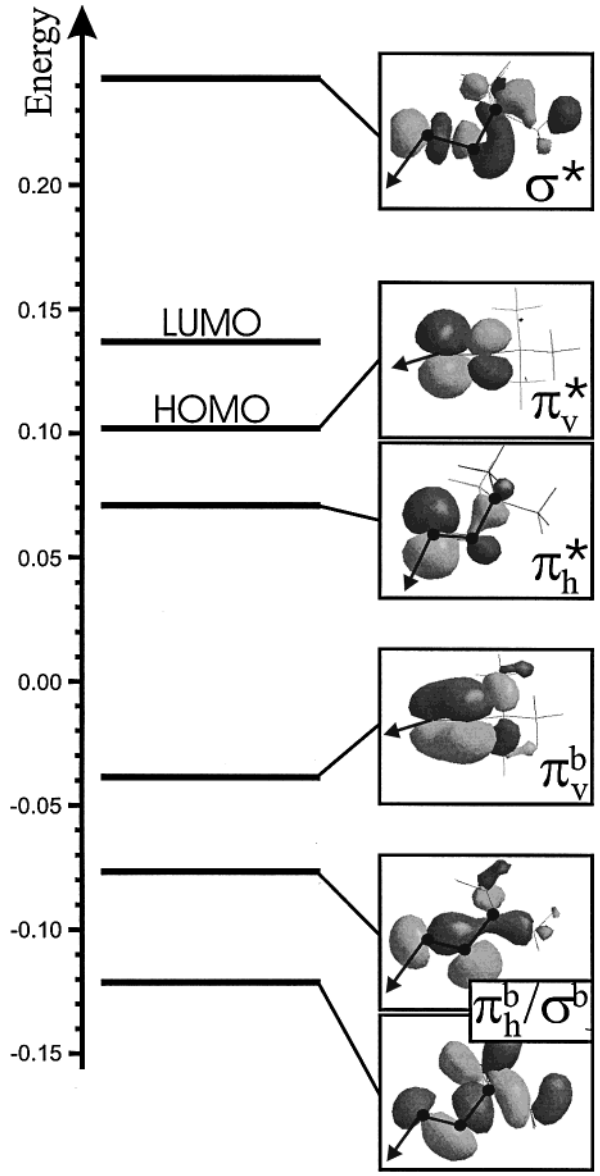

Figure 1. Molecular orbitals of the free $^tBuOO^-$ ligand. For all the orbitals that lie within the O−O−C_{3t} plane (C_{3t} denotes the central carbon of the *tert*-butyl group), the positions of these three atoms are indicated by black spheres. The direction of interaction with iron is given by the arrow (note that in the geometry optimized structures, the Fe−O−O−C_{3t} dihedral angle is about 180° such that these four atoms form a plane).

Experimental and Computational Procedures

The Fe(III)−alkylperoxo complex **1** was prepared in different solvents following the general procedure described in ref 32 as required by the different spectroscopic methods (vide infra).

UV−Vis Spectroscopy. Absorption spectra have been recorded in acetonitrile solution at −40 °C on a Hewlett-Packard 8452 diode array spectrophotometer. For the low-temperature measurements, an immersion dewar equipped with quartz windows and filled with methanol cooled by liquid N_2 was used.

Raman Spectroscopy. The resonance Raman spectra presented in Figure 2 (vide infra) have been measured at an excitation wavelength of 600 nm (615 nm for the ^{54}Fe data) in frozen acetonitrile solutions at 77 K. A Spex 1403 double monochromator interfaced with a Spex DM3000 data system was used together with a Spectra Physics 2030-

(59) MacFaul, P. A.; Ingold, K. U.; Wayner, D. D. M.; Que, L., Jr. *J. Am. Chem. Soc.* **1997**, *119*, 10594−10598.

(60) Lange, S. J.; Miyake, H.; Que, L., Jr. *J. Am. Chem. Soc.* **1999**, *121*, 6330−6331.

15 argon ion laser to pump a 375B CW dye laser (rhodamine 6G). Samples were frozen onto a gold-plated copper coldfinger in thermal contact with a dewar containing liquid N_2 [61] and measured in a backscattering geometry.

For the resonance Raman profiles (Figures 4 and 5), a series of excitation wavelengths of a krypton ion (Coherent 190C-K) and an argon ion (Coherent Sabre 25/7) laser have been used at incident powers of about 25 mW and in a ~135° backscattering geometry. A Spex 1877 CP triple monochromator (equipped with 1200, 1800, and 2400 groves/mm gratings) has been used together with a back-illuminated CCD camera (Princton instruments CCD-1100PB) as a detector. Samples were prepared in acetonitrile in NMR tubes and measured at 77 K in a quarz EPR dewar cooled by liquid N_2. Raman intensities were internally calibrated to the intense 922 cm^{-1} vibration of the solvent acetonitrile. Sample concentrations were in the range of ~10 mM.

MCD Spectroscopy. MCD spectra have been obtained on frozen glasses of butyronitrile solutions at liquid He temperatures (1.8−25 K). A CD spectropolarimeter (Jasco 810) with S1 and S20 photomultiplier tubes as detectors has been used where the sample compartment was modified to accommodate an Oxford instruments SM4-7T magnetocryostat. The samples were frozen in metallic sample compartments between two Infrasil quartz disks separated by 3 mm neoprene spacers. Typical sample concentrations were in the range of 0.2−1.0 mM.

Data Analysis. Normal coordinate calculations were performed using the QCPE computer program 576 by M. R. Peterson and D. F. McIntosh, which involves solution of the secular equation $\mathbf{GFL} = \lambda\mathbf{L}$ by the diagonalization procedure of Miyazawa.[62] The calculations are based on a general valence force field; force constants are refined with the nonlinear optimization routine of the simplex algorithm according to Nelder and Mead.[63] The simplex optimization was always used to refine only *selected* force constants according to the quantum-chemical assisted normal coordinate analysis that has been applied.[64] Here, a force field from DFT calculations is used as a starting point to generate initial force constants and a subset of these is fit to reproduce the known experimental frequencies.

For the Heller simulations[65−68] of the resonance Raman profiles and absorption bands a MathCad 7.0 script written by Dr. Thomas Brunold was used.[69]

Density Functional Calculations. Spin-unrestricted DFT calculations using Becke's three-parameter hybrid functional with the correlation functional of Lee, Yang, and Parr (B3LYP[70−72]) were performed using the program package Gaussian 94/98.[73] The structures of the three Fe(III)−alkylperoxo model systems (cf. Table 6), the three Fe^{IV}═O(OH) (S = 0, 1, 2; cf. Table 10) and two Fe^{IV}═$O(OH_2)$ (S = 1, 2) intermediates, the •O^{t}Bu radical, and H_2O_2, $^-$OOH, $(O_2)^{2-}$, HOO^{t}Bu, and $^-$OO^{t}Bu (cf. Table 7) were fully optimized with the LanL2DZ basis set and frequencies and force constants as well as thermodynamic parameters have been calculated. Note that the obtained structure for model system low-spin $[Fe(NH_3)_4(OH_2)(OO^tBu)]^{2+}$ ($\tilde{\mathbf{1}}$) has one imaginary frequency ($|\tilde{\nu}| < 20$ cm^{-1}) corresponding to an Fe−NH_3 rotation which, however, is not significant for the analyses presented here. The LanL2DZ basis set applies Dunning/Huzinaga full double-ζ (D95)[74] basis functions on first row and Los Alamos effective core potentials plus DZ functions on all other atoms.[75,76] For the calculations of reaction energies, a triple-ζ valence basis set of Ahlrichs and co-workers[77] (TZV; used as implemented in the G98 program package) has also been applied on the LanL2DZ structures. TZV+ adds additional diffuse functions on the heavy atoms. Solvation effects were included in the calculations using the Polarized Continuum Model (PCM)[78] and with acetonitrile as the solvent. In all these calculations, convergence was reached when the relative change in the density matrix between subsequent iterations was less than 1×10^{-8}. Force constants in internal coordinates were extracted from the Gaussian output using the program Redong[79] (QCPE 628).

Spin-unrestricted calculations to obtain the MO diagrams of $\tilde{\mathbf{1}}$ (Figure 6 and Table 8) and $\tilde{\mathbf{2}}$ (Figure 9 and Table 11) were performed with the Amsterdam Density Functional (ADF) program version 2.0.1[80,81] using the local density approximation (LDA) together with gradient corrections for exchange (Becke88[82]) and correlation (Perdew86[83]). An uncontracted valence triple-ζ Slater-type basis set was used (ADF basis set IV) for all atoms with an additional set of f functions on iron. Core orbitals were frozen through 1s (C, N, O) and 3p (Fe) in the calculations. Orbitals in Figures 7 and 8 were plotted with the program Cerius2.

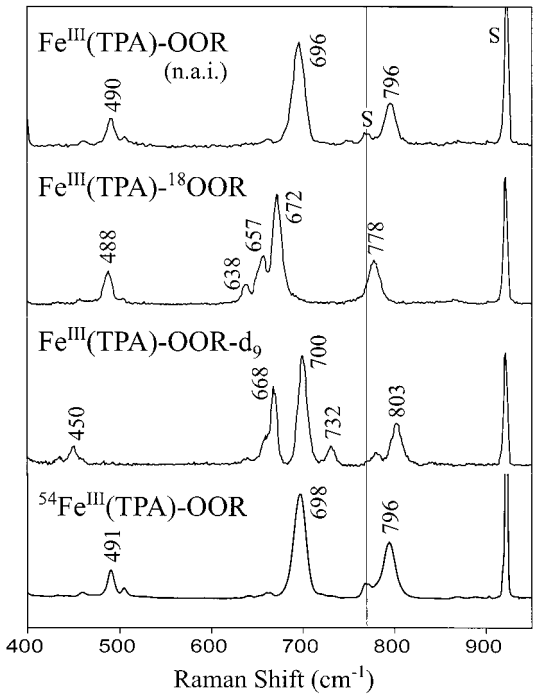

Figure 2. Resonance Raman spectra of **1**. From top to bottom: natural abundance isotopes (n.a.i.) spectrum; ^{18}O substituted ligand at the coordinating oxygen; ligand with fully deuterated *tert*-butyl group; and ^{54}Fe substitution. The spectra were recorded at 77 K at an excitation wavelength of about 600 nm in acetonitrile.

Results and Analysis

(A) Spectroscopy. (1) Resonance Raman Spectra and Vibrational Analysis. (a) Vibrational Assignment. Figure 2

(61) Czernuszewicz, R. C.; Johnson, M. K. *Appl. Spectrosc.* **1983**, *37*, 297−298.
(62) Miyazawa, T. *J. Chem. Phys.* **1958**, *29*, 246.
(63) Nelder, J. A.; Mead, R. *Comput. J.* **1965**, *7*, 308.
(64) Lehnert, N.; Tuczek, F. *Inorg. Chem.* **1999**, *87*, 1659−1670.
(65) Lee, S. Y.; Heller, E. J. *J. Chem. Phys.* **1979**, *71*, 4777.
(66) Tannor, D. J.; Heller, E. J. *J. Chem. Phys.* **1982**, *77*, 202.
(67) Myers, A. B.; Mathies, R. A. *Resonance Raman Intensities: A Probe of Excited-State Structure and Dynamics*; Spiro, T. G., Ed.; John Wiley: New York, 1987; Vol. 2, pp 1−58.
(68) Zink, J. I.; Shin, K.-S. K. *Adv. Photochem.* **1991**, *16*, 119−214.
(69) Brunold, T. C.; Tamura, N.; Kitajima, N.; Moro-oka, Y.; Solomon, E. I. *J. Am. Chem. Soc.* **1998**, *120*, 5674−5690.
(70) Becke, A. D. *Phys. Rev. A* **1988**, *38*, 3098.
(71) Becke, A. D. *J. Chem. Phys.* **1993**, *98*, 1372.
(72) Becke, A. D. *J. Chem. Phys.* **1993**, *98*, 5648.
(73) Frisch, M. J.; Trucks, G. W.; Schlegel, H. B.; Gill, P. M. W.; Johnson, B. G.; Robb, M. A.; Cheeseman, J. R.; Keith, T. A.; Petersson, G. A.; Montgomery, J. A.; Raghavachari, K.; Al-Laham, M. A.; Zakrzewski, V. G.; Ortiz, J. V.; Foresman, J. B.; Cioslowski, J.; Stefanov, B. B.; Nanayakkara, A.; Challacombe, M.; Peng, C. Y.; Ayala, P. Y.; Chen, W.; Wong, M. W.; Andres, J. L.; Replogle, E. S.; Gomperts, R.; Martin, R. L.; Fox, D. J.; Binkley, J. S.; Defrees, D. J.; Baker, J.; Stewart, J. P.; Head-Gordon, M.; Gonzalez, C.; Pople, J. A. *Gaussian 94/98*; Gaussian, Inc.: Pittsburgh, PA, 1995.
(74) Dunning, T. H., Jr.; Hay, P. J. *Modern Theoretical Chemistry*; Schaefer, H. F., III. Ed.; Plenum: New York, 1976.
(75) Hay, P. J.; Wadt, W. R. *J. Chem. Phys.* **1985**, *82*, 270 and 299.
(76) Wadt, W. R.; Hay, P. J. *J. Chem. Phys.* **1985**, *82*, 284.
(77) Schafer, A.; Huber, C.; Ahlrichs, R. *J. Chem. Phys.* **1994**, *100*, 5829.
(78) Cramer, C. J.; Truhlar, D. G. *Chem. Rev.* **1999**, *99*, 2161−2200.
(79) Allouche, A.; Pourcin, J. *Spectrochim. Acta* **1993**, *49A*, 571.
(80) Baerends, E. J.; Ellis, D. E.; Ros, P. *J. Chem. Phys.* **1973**, *2*, 42.
(81) te Velde, G.; Baerends, E. J. *J. Comput. Phys.* **1992**, *99*, 84.
(82) Becke, A. D. *J. Chem. Phys.* **1986**, *84*, 4524.
(83) Perdew, J. P.; Chevary, J. A.; Vosko, S. H.; Jackson, K. A.; Pederson, M. R.; Singh, D. J.; Fiolhais, C. *Phys. Rev. A* **1992**, *46*, 6671.

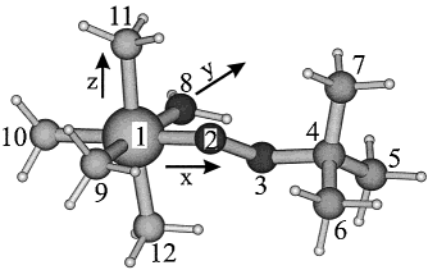

Figure 3. Optimized structure (B3LYP/LanL2DZ) of the simplified model system $\tilde{\mathbf{1}}$ in which the TPA ligand (having three pyridines and one tertiary amine donor) has been replaced by four ammonias. A water is used as the sixth ligand to the iron center. The coordinates of $\tilde{\mathbf{1}}$ are given in the Supporting Information, Table 1. Important structural parameters (bond lengths in Å, angles in deg): Δ(Fe−O) = 1.818; Δ(O−O) = 1.488; Δ(C−O) = 1.565; Fe−O−O = 111; C−O−O = 112; Fe−O−O−C = 176. The 12 heavy atoms of this system comprise the model used for NCA ($\hat{\mathbf{1}}$) with the indicated numbering of the atoms.

shows the resonance Raman spectra of low-spin [Fe(TPA)-$(OH_x)(OO^tBu)]^{x+}$ (**1**) recorded with a laser wavelength of 599.5 nm exciting into the broad absorption band around 600 nm (vide infra, UV−vis spectrum in Figure 4). In the natural abundance isotopes (n.a.i.) spectrum (top panel), three features are observed at 796, 696, and 490 cm^{-1} that shift down to 778, 672, and 488 cm^{-1} on ^{18}O substitution of the coordinating oxygen. The two additional features at 657 and 638 cm^{-1} in the isotope pertubed spectrum are also present in the n.a.i. data but with much less intensity. When the 696 cm^{-1} feature shifts to 672 cm^{-1} the energy difference to the two peaks at 657 and 638 cm^{-1} gets much smaller which increases mode mixing and allows the two weak peaks to gain intensity from the 672 cm^{-1} mode. On deuteration of the *tert*-butyl group the three features in the n.a.i. spectrum shift to 803, 700, and 450 cm^{-1} and new features appear at 732 and 668 cm^{-1}. These results have been previously reported.[32] The bottom panel shows the spectrum where the iron has been substituted with the ^{54}Fe isotope. Small shifts are observed for the two lower energy features placing them at 698 and 491 cm^{-1}. On the basis of the assignment of the 600 nm absorption as an alkylperoxo to Fe(III) charge-transfer transition (vide infra), one would expect that the excited state distortions mainly occur along the O−O and Fe−O stretching coordinates. This would lead to two resonance enhanced vibrations rather than the three observed in the n.a.i. spectrum in Figure 2.

To address this problem, a normal coordinate analysis (NCA) has been performed on a simplified model of **1**. As the crystal structure of **1** is not known, a structure was estimated from density functional calculations that will be presented in Part B. A simplified model of **1** having the three pyridine donors of the TPA ligand substituted by NH_3 and a water molecule as the sixth ligand ($\tilde{\mathbf{1}}$) was geometry optimized and the resulting structure is shown in Figure 3. For the NCA, all hydrogen atoms are neglected leading to model $\hat{\mathbf{1}}$ consisting of the 12 heavy atoms of $\tilde{\mathbf{1}}$ (cf. Figure 3). Effective masses reflecting the TPA ligand are used for the nitrogens ($M = 50$ for N_9, $M = 74$ for $N_{10}-N_{12}$) of $\hat{\mathbf{1}}$ and masses of 15 have been applied to the carbons of the CH_3 groups (C_5-C_7). Additional problems associated with the NCA of this system are that the vibrations of the *tert*-butyl group strongly mix with the O−O and Fe−O vibrations and that the C−O stretching vibration will also interact with these modes, but all the corresponding coupling elements of the **f** matrix are unknown. To solve the NCA for this highly coupled system, a Quantum Chemistry Assisted Normal Coordinate Analysis (QCA-NCA)[64] approach has been applied. In this method, a simplified form of the quantum chemical derived force field of $\tilde{\mathbf{1}}$ is used as a first approximation in NCA and then selected force constants are fitted to reproduce the experimental results. Table 1 gives the force constants of the Fe−O−O^{t}Bu subunit of $\hat{\mathbf{1}}$ before (column labeled: calc ($x = 2$)) and after (QCA-NCA ($x = 2$)) fitting to the experimental data and, for comparison, the calculated force field of the complex with hydroxide as the sixth ligand ($\tilde{\mathbf{1}}\mathbf{a}$; calc ($x = 1$) in Table 1). The potential energy distributions (ped) from the QCA-NCA fit of $\hat{\mathbf{1}}$ for the n.a.i. complex and the two *tert*-butylperoxo isotope substituted species are given in Table 2 along with a comparison of the experimental and predicted vibrational energies.

Table 1. Calculated (B3LYP/LanL2DZ) and Experimental (QCA-NCA) Force Constants

			low-spin $[Fe(NH_3)_4(OH_x)(OO^tBu)]^{x+}$		
no.		force constant[a]	calc ($x = 2$)	calc ($x = 1$)	QCA-NCA ($x = 2$)
1	X	Fe−O	3.3830	2.8869	3.5281
22	Z	O−O	3.3853	3.4692	2.9181
23	Y	C−O	2.4314	3.4604	2.8301
24	S_{co}	O−O/C−O	0.3319	0.2783	0.2687
25	C	C−C	⟨4.47⟩[c]	⟨4.40⟩[c]	4.8883[b]
27	Q	Fe−O−O	1.8664	1.3846	1.3765
28	R	C−O−O	1.1710	1.2957	1.2344
58	D1	$O-C-C_5$	1.0964	1.1153	1.0964
59	D2	$O-C-C_6$	1.0758	1.0782	1.0758
60	D3	$O-C-C_7$	1.0775	1.0939	1.0775
61	E1	C_5-C-C_6	0.8871	0.9157	0.8871
62	E2	C_5-C-C_7	0.8852	0.9223	0.8852
63	E3	C_6-C-C_7	0.8055	0.8326	0.8055
67	S_{FeO}	Fe−O/O−O	0.5283	0.2690	0.4163
69	S_{FeC}	Fe−O/C−O	0.0181	0.0521	-0.1158
70	32	C−O/C−C	⟨0.275⟩[c]	⟨0.280⟩[c]	0.2900
71	B_{Fe}	Fe−O/Fe−O−O	0.9094	0.6944	0.7745
73	B_{FeO}	O−O/Fe−O−O	0.5875	0.3620	0.4259
74	B_{FeC}	C−O/Fe−O−O	0.0287	0.0400	-0.0391
75	B_{CFe}	Fe−O/C−O−O	0.0063	0.0513	-0.0450
76	B_{CO}	O−O/C−O−O	0.2812	0.2998	0.1754
77	B_C	C−O/C−O−O	0.1998	0.3012	0.1489
112	K1	$O-O/C-C_5$	−0.0574	−0.0600	-0.1176
113	K2	$O-O/C-C_{6/7}$	⟨0.012⟩[c]	⟨0.013⟩[c]	0.0200
114	K3	$Fe-O/O-C-C_{6/7}$	⟨0.011⟩[c]	⟨−0.003⟩[c]	0.0391
127	K4	$Fe-O/O-C-C_5$	0.0011	0.0073	-0.0081

[a] Units of force constants are mdyn/Å for stretching, mdyn·Å for bending, and mdyn for stretch−bend interactions. [b] Effective force constant used to adjust the C−C stretches (otherwise they are too low in energy since masses of 15 have been used for the carbons in the NCA; this strategy was preferred to adjusting the carbon masses to values between 14 and 15). [c] ⟨...⟩: force constant averaged over all corresponding coordinates.

The results from NCA unequivocally allow the assignment of the three features observed in the resonance Raman spectrum of **1** in Figure 2, top. In the n.a.i. compound, the 796 cm^{-1} feature is assigned to the O−O stretching vibration ν(OO) and the 696 cm^{-1} band to the Fe−O stretch ν(FeO). The peak at 490 cm^{-1} is identified as a combined δ(OCC)/δ(CCC) bending vibration that is mixed with ν(FeO) and this mixture is the source of the resonance Raman intensity of this mode. As indicated in Table 2 (n.a.i.), there are four δ(OCC)/δ(CCC) bends located in the region between 470 and 550 cm^{-1} in the NCA (in square brackets), whereas in the DFT calculation of model $\tilde{\mathbf{1}}$ the first mode appears at 469 cm^{-1} using the same set of diagonal force constants in the **f** matrix (cf. Table 1: D1−D3 and E1−E3). This is due to the fact that the NCA simulation lacks the hydrogens at the three terminal carbon atoms. The DFT calculations show that the O−C−C and C−C−C bends also mix with C−C−H bends. Since these coordinates are

Table 2. Comparison of Experimental and QCA-NCA (and DFT) Frequencies and Potential Energy Distributions[a]

exp. freq		QCA-NCA (DFT)	potential energy distribution							
			ΔFe−O	ΔO−O	ΔC−O	ΔC−C	ΔFe−O−O	ΔC−O−O	∠O−C−C	∠C−C−C
						$Fe-^{16}O-^{16}O-C(^{15}C)_3$ (n.a.i.)				
		883	0	2	27	55	1	0	9	5
796		796	5	72	11	1	1	2	5	0
∼750		756	9	1	33	17	17	18	3	1
696		696.00	61	0	16	6	4	6	3	1
490		[551][b]	13	0	2	6	2	6	42	24
		[512][b]	0	0	0	8	0	0	50	28
		[501][b]	2	1	0	4	20	1	14	14
		[477][b]	0	0	0	1	0	0	3	10
	DFT	469[c]	8	0	9	2	1	8	35	18
		447[c]	0	0	0	3	1	0	45	20
						$Fe-^{18}O-^{16}O-C(^{15}C)_3$				
		882	0	1	28	56	1	0	9	5
778		777	3	72	14	0	0	2	5	0
−		750	3	3	37	19	15	17	3	1
672		673	65	0	9	5	5	8	4	1
488		[549][b]	16	0	2	6	2	6	41	24
		[511][b]	0	0	0	8	0	0	51	29
		[496][b]	2	1	0	3	19	0	11	13
		[475][b]	1	0	0	2	0	0	4	13
	DFT	467[c]	10	0	9	2	0	6	35	19
		447[c]	0	0	0	3	1	1	47	21
						$Fe-^{16}O-^{16}O-C(^{18}C)_3$				
		854	0	2	37	40	2	1	11	6
803		796	5	70	13	1	1	1	5	0
732		736	21	2	13	20	20	21	2	0
⟨685⟩		684	57	0	20	16	1	2	1	0
450		[528][b]	9	0	3	11	2	6	40	22
		[492][b]	1	0	0	2	15	1	7	3
		[488][b]	1	0	0	7	0	0	35	15
		[469][b]	1	0	0	4	1	1	14	11
	DFT	419[c]	5	0	7	2	5	9	25	7
		401[c]	0	0	0	2	1	1	52	10

[a] Experimental (and NCA) results for $^{54}Fe-^{16}O-^{16}O-C(^{15}C)_3$ are (in cm^{-1}/n.o. = not observed): n.o. (883)/796 (796)/n.o. (756)/698 (698.01)/491 ([552, 512, 504, 481]). For $Fe-^{18}O-^{18}O-C(^{15}C)_3$, the following energies are predicted by NCA (the type of stretching vibration is in parentheses): 880 (C−C)/ 752 (O−O)/ 728 (C−O)/ 671 (Fe−O)/[543, 504, 494, 475]. [b] Not fit; this region is cleaned up by interaction of the O−C−C/C−C−C bends with C−C−H bends which causes the δ(OCC)/δ(CCC) modes to shift to lower energy as can be seen from the DFT results. [c] The two O−C−C/C−C−C bends at highest energy in the DFT calculation of **1̃**. The remaining bends at lower energy do not show any admixture from ΔFe−O and ΔO−O.

missing, the NCA cannot accurately describe the O−C−C/C−C−C bending modes and therefore they are not included in the fitting procedure (only nondiagonal elements K_3 and K_4 are floated, cf. Table 1). Altogether, six O−C−C and C−C−C coordinates are needed corresponding to five actual vibrations and one redundacy. The fact that only one of these five modes is experimentally observed in the Raman spectra indicates that, while the intrinsic O−C−C and C−C−C coordinates have no resonance intensity, the 490 cm^{-1} vibration selectively mixes with ν(FeO) (and ν(OO); this, however, is small due to the large energy separation) to get intensity. Further support for this assignment comes from the isotope-labeled spectrum with the deuterated *tert*-butyl group (cf. Figure 2, panel 3 and vide infra) where the vibration at 490 cm^{-1} is shifted by −40 cm^{-1}. Other important features in the NCA (cf. Table 2) are the symmetric C−C stretch and the C−O stretch which are strongly mixed. The feature at 883 cm^{-1} has more C−C stretching character and is therefore designated as ν_s(CC) whereas ν(CO) is located at 756 cm^{-1} in the simulation. Note that there is a weak feature around 750 cm^{-1} in the Raman spectrum that can tentatively be assigned to ν(CO) and whose intensity arises from mixing with ν(FeO) (9% in the NCA).

The assignment of the 490 cm^{-1} vibration as an O−C−C/C−C−C bend is in agreement with the DFT calculation of **1̃**. Since the calculation was performed on the whole *tert*-butyl group including the hydrogen atoms, a more accurate describtion of the five δ(OCC)/δ(CCC) modes is obtained. Here, the bending vibration at 469 cm^{-1} is mixed with ν(FeO) whereas the modes at lower energy are not (a representative mode at 447 cm^{-1} is included in Table 2). Nevertheless, the large experimental intensity of the 490 cm^{-1} peak shows that the mixing of 8% ΔFe−O calculated with DFT is an underestimate (from the Heller analysis of the resonance Raman profiles the admixture is about 39% (vide infra)).

The observed shifts of both ν(OO) and ν(FeO) on ^{18}O substitution of the coordinating oxygen are well reproduced by the NCA. Because of the shift of ν(FeO) to lower energy, mode mixing with ν(CO) gets smaller (only 3% ΔFe−O), which explains why this mode (∼750 cm^{-1}) disappears in the ^{18}O labeled spectrum. The shift of the δ(OCC)/δ(CCC) bend is also reproduced in the simulation. As already indicated, the modes at 657 and 638 cm^{-1} gain intensity on ^{18}O substitution because of the shift of ν(FeO) to lower energy.

In addition to the low-energy shift of the 490 cm^{-1} mode, two new features appear in the spectrum at 732 and 668 cm^{-1} (cf. Figure 2) upon deuteration of the *tert*-butyl group. The presence of the 668 cm^{-1} feature reflects the fact that the C−C−H bending vibrations shift down into the 700−900 cm^{-1} region on deuteration. One of these modes which is close in energy to ν(FeO) could strongly mix with this vibration and gain intensity. The true position of ν(FeO) for the NCA is then the intensity weighted average position of the bands at 668 and 700 cm^{-1}. This puts ν(FeO) in the region of 685−690 cm^{-1}. The fact that ν(OO) shifts up in energy by 7 cm^{-1} is also

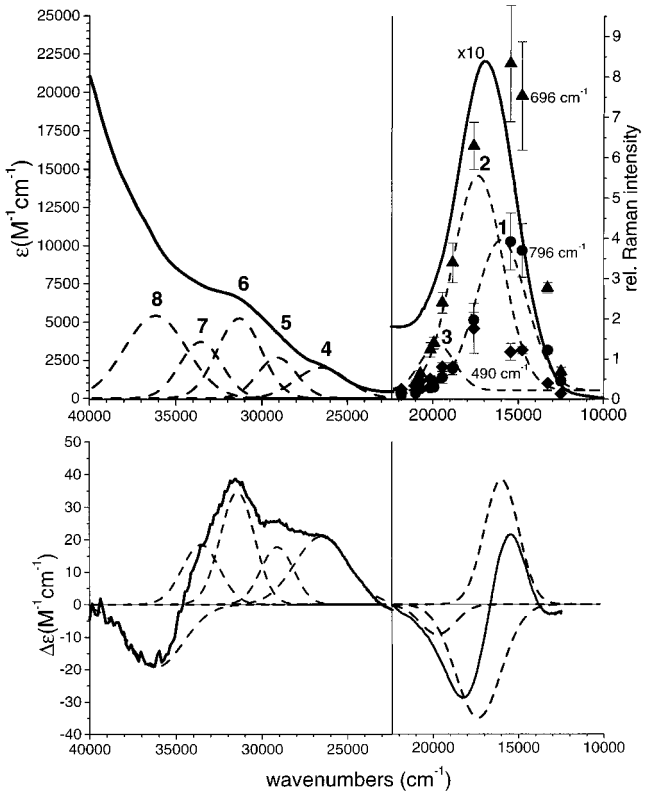

Figure 4. UV−vis (top) and MCD spectra (bottom, recorded at 5 K and 7 Tesla) of **1** together with simultaneous Gaussian fits (bands 1−8). The low energy range of the UV−vis spectrum (top, right) is enlarged by a factor of 10 ($\epsilon = 2200$ M^{-1} cm^{-1}). This panel also contains the resonance Raman profiles of ν(FeO) (▲; 696 cm^{-1}), ν(OO) (●; 796 cm^{-1}), and δ(OCC/CCC) (◆; 490 cm^{-1}).

consistent with a shift of the C−C−H bends from higher energy into the 700−900 cm^{-1} region. In this case, a small interaction shifts the O−O stretch to 803 cm^{-1} whereas the corresponding bend is located around 780 cm^{-1} overlaying the solvent peak at 770 cm^{-1} as indicated in Figure 2. As the C−C−H bends are not included in the simulation (vide supra), the NCA shifts ν(FeO) to 684 cm^{-1} in agreement with the averaged position in the Raman spectrum, whereas no shift occurs for ν(OO). Note that the C−O stretch gains significant intensity on deuteration since it shifts down to 736 cm^{-1} in the simulation and mixes with ν(FeO) (21% vs 9% in the n.a.i. case, cf. Table 2). This is in agreement with the observed new feature at 732 cm^{-1} in the Raman spectrum (Figure 2, panel 3). The large shift on deuteration observed for the 490 cm^{-1} peak is well reproduced by the DFT calculation. Note that this feature loses intensity in the deuterated spectrum compared to the n.a.i. case due to the larger energetic separation to ν(FeO) which decreases mode mixing.

The 2 cm^{-1} shift of ν(FeO) to higher energy in the ^{54}Fe complex is well reproduced in the NCA as given in the footnote of Table 2 (here, the potential energy distribution (ped) matrix does not change relative to the n.a.i. case).

(b) Analysis of Force Constants. Table 1 gives a list of the force constants of the Fe−O−O−C(C_3) subunit of $\hat{\mathbf{1}}$ (the complete **f** matrix is given in the Supporting Information, Tables 4 and 5). The starting point for the NCA is model $\tilde{\mathbf{1}}$, the calculated force constants of which are shown in Table 1, left (calc: $x = 2$), and the final values after fitting to the experimental data are given in Table 1, right (QCA-NCA: $x = 2$). The changes for diagonal elements are within ±0.5 and for nondiagonal elements within ±0.15. The most striking result from the QCA-NCA is that complex **1** has a very strong Fe−O bond ($k = 3.53$ mdyn/Å) whereas the O−O ($k = 2.92$ mdyn/Å) and C−O ($k = 2.83$ mdyn/Å) bonds are weak. Both the Fe−O−O and the C−O−O angle bends have force constants of about the same magnitude ($k = 1.38$ vs 1.23 mdyn·Å). The large nondiagonal element between the Fe−O and the O−O stretch illustrates the sensitivity of the Fe−O bond strength to changes along the O−O coordinate: when the O−O distance is varied during the time course of the O−O stretch, the peroxide-based donor orbitals change in energy and this directly influences the Fe−O bond. Other large off-diagonal elements of the **f** matrix are found between the Fe−O−O bend and the Fe−O and the O−O stretch: a change in the Fe−O−O angle mainly leads to changes in the σ bond between iron(III) and the peroxide ligand by altering the overlap of the corresponding orbitals and this has a large influence on the Fe−O and O−O bond strength. All the other nondiagonal elements from the QCA-NCA procedure (cf. Table 1) have absolute values smaller than |0.3|.

A.2. UV−Vis Absorption, MCD, and Resonance Raman Profiles. The absorption spectrum of **1** is shown in Figure 4, top. One broad absorption is observed in the visible region around 16800 cm^{-1} (600 nm; $\epsilon = 2200$ M^{-1} cm^{-1}). Above 25000 cm^{-1} the extinction continuously increases with two shoulders around 26 000 and 31 000 cm^{-1}, but no distinct absorption feature appears at higher energy. The MCD spectrum shown in Figure 4 (bottom) is much better resolved and allows the identification of three transitions under the broad envelope of the 600 nm absorption band. In the high-energy region, five more transitions can clearly be identified in the MCD data. The eight dashed Gaussian bands in Figure 4 are simultaneous fits of the absorption and MCD spectra using the same band positions but different half widths since the spectra have been recorded at different temperatures and under different conditions (solution vs frozen glass, cf. Experimental Section). Table 3 lists the resulting parameters of the eight fitted Gaussians. The two intense MCD features at lower energy (bands 1 and 2) have very similar MCD intensities but show a sign change from + to − like a derivative shaped MCD **A** term signal. Nevertheless, these two bands are temperature dependent and therefore clearly have MCD **C** term character and correspond to two electronic transitions (vide infra). Such a MCD feature has been designated as pseudo-**A** term.[84−87] The third, much weaker MCD signal (band 3) in the region of the 600 nm absorption has a negative sign and is centered at 19723 cm^{-1} in the fit. At higher energy, four positive **C** terms are required between 25 000 and 35 000 cm^{-1} (bands 4−7) followed by a negative feature (band 8) centered at 36173 cm^{-1}.

Figure 4 (top) also contains the resonance Raman profiles of the O−O stretch (796 cm^{-1}), the Fe−O stretch (696 cm^{-1}), and the OCC/CCC bend (490 cm^{-1}), which has a large ν(FeO) admixture (vide supra). All three vibrations are clearly resonance enhanced with respect to the 600 nm absorption. Hence, the main displacement of the excited state (relative to the ground state) occurs along the ΔO−O and ΔFe−O stretching coordinates. In accordance with the DFT calculations (vide infra), the 600 nm absorption can therefore be assigned as a charge-transfer transition from the alkylperoxo HOMO π_v^* (cf. Figure 1) to the singly occupied t_{2g} orbital of low-spin Fe(III) ($[t_{2g}]^5$ ground state electron configuration). From the simultaneous fit of the

(84) Stephens, P. J. *J. Chem. Phys.* **1970**, *52*, 3489.
(85) Stephens, P. J. *Annu. Rev. Phys. Chem.* **1974**, *25*, 201.
(86) Stephens, P. J. *Adv. Chem. Phys.* **1976**, *35*, 197.
(87) Neese, F.; Solomon, E. I. *Inorg. Chem.* **1999**, *38*, 1847−1865.

Table 3. Result of the Simultaneous Gaussian Fit of the Absorption and MCD Spectrum

band	ν_{max} (cm^{-1})	ϵ_{max} ($M^{-1}cm^{-1}$)	$\Delta\epsilon_{max}$ ($M^{-1}cm^{-1}$)	f [a]	$\lvert\Delta\epsilon/\epsilon\rvert$
1	16000	1008	39	0.01607	0.039
2	17364	1438	−35	0.02255	0.024
3	19723	308	−9	0.00333	0.029
4	26513	2014	21	0.03272	0.010
5	29107	2680	18	0.03280	0.007
6	31316	5246	35	0.07289	0.007
7	33556	3701	19	0.04870	0.005
8	36173	5416	−19	0.10556	0.004

[a] f = oszillator strength.

absorption and MCD data, the 600 nm absorption has been resolved into two intense and one weak transition (bands 1−3). This result together with the broad appearance of the resonance profiles indicates that the CT character is distributed over bands 1 and 2. Further evidence for this assignment comes from the Heller fit of the resonance profiles: these have asymmetric shapes (cf. Figure 5) that can only be reproduced when fit with two absorptions having about the same CT character (vide infra). Therefore, two transitions with CT character contribute to the 600 nm absorption band which give rise to a pseudo-**A** signal in the MCD spectrum.

(a) Analysis of the Pseudo-A Term. The mechanism that leads to the equal distribution of the CT intensity over two bands and the pseudo-**A** term in the MCD spectrum is now evaluated. In the domain where the MCD signal is a linear function of the applied magnetic field, the total MCD intensity for samples of randomly oriented molecules is given by:[84−86]

$$\frac{\Delta\epsilon}{E} = \gamma\cdot\beta\cdot B\left[\mathbf{A}_1\left(\frac{-\partial f(E)}{\partial E}\right) + \left(\mathbf{B}_0 + \frac{\mathbf{C}_0}{kT}\right)f(E)\right]$$

with γ being a collection of constants; β is the Bohr magneton and B is the magnetic flux density; k is the Boltzmann constant; T is the absolute temperature; the $\mathbf{A}_1$, $\mathbf{B}_0$, and $\mathbf{C}_0$ terms define three different types of MCD mechanisms and the $f(E)$ is a band shape function. **C** term intensity arises from species with paramagnetic ground states and usually dominates the low-temperature spectra of such systems due to the $1/kT$ dependence. For an $S = {}^1/_2$ (orbitally nondegenerate) ground state and including an explicit treatment of spin-allowed transitions, the $\mathbf{C}_0$ term intensity is defined by:[87]

$$\mathbf{C}_0 = -\frac{1}{6}\sum_{uvw}\epsilon_{uvw}g_w\sum_{K\neq A,J}\{\Delta_{KJ}^{-1}(\vec{\mathrm{D}}_u^{KA}\times\vec{D}_v^{AJ})\cdot\bar{L}_w^{KJ} + \Delta_{KA}^{-1}(\vec{D}_u^{AJ}\times\vec{\mathrm{D}}_v^{JK})\cdot\bar{L}_w^{KA}\} \quad (1)$$

for a transition from the ground state $|A\rangle$ to the excited state $|J\rangle$. Here, ϵ_{uvw} is the Levi−Civita symbol with $(u,v,w) = (x,y,z)$; g_w are the g-values of the molecule; the $\sum_K$ runs over all other excited states $|K\rangle \neq |J\rangle$ which are intermediate states; $\Delta_{KJ} = E_K - E_J$ is the energy denominator (from second-order perturbation theory); $\vec{\mathrm{D}}_u^{KA}$, for example, is the transition dipole moment for a transition between the states $|A\rangle$ and $|K\rangle$ in direction u and

$$\bar{L}_w^{KJ} = \mathrm{Im}\langle K\mathrm{SM}_S^K|\boldsymbol{H}_{SOC}^w|J\mathrm{SM}_S^J\rangle$$

for example, is the spin−orbit coupling (SOC) matrix element between states $|K\rangle$ and $|J\rangle$. Equation 1 describes two different mechanisms contributing to **C** term intensity as shown in Scheme 1. Either the ground state $|A\rangle$ (Scheme 1, right) or the excited state $|J\rangle$ (Scheme 1, left) spin−orbit couples to an intermediate state $|K\rangle$. For MCD intensity to arise, the spin−orbit coupling has to be effective in a direction orthogonal to the plane formed by the two transition dipole moments $\vec{D}$. Moreover, if these transition dipole vectors are collinear, the MCD intensity vanishes. Besides these strict selection rules for **C** terms resulting from the vector product $(\vec{D}_u\times\vec{D}_v)\cdot\bar{L}_w$, the energy of the state $|K\rangle$ is important because of the energy denominator Δ^{-1} in eq 1. Importantly, only the first mechanism in eq 1 (cf. Scheme 1, left) where the intermediate state $|K\rangle$ is close in energy to $|J\rangle$ gives rise to pseudo-**A** terms in the MCD spectrum.[88] Here, the two excited states $|J\rangle$ and $|K\rangle$ spin−orbit couple and the two transition dipole moments correspond to the two actual transitions from $|A\rangle$ to $|J\rangle$ and $|K\rangle$ (Scheme 1,

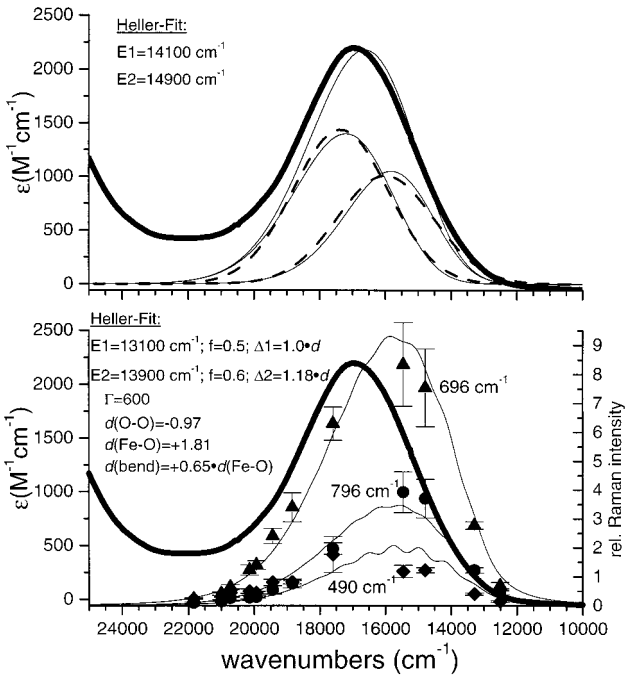

Figure 5. Heller fit of the absorption spectrum (top; the dashed lines are bands 1 and 2 from the simultaneous fit of the absorption and MCD data) and the resonance Raman profiles (bottom) of ν(FeO) (▲; 696 cm^{-1}), ν(OO) (●; 796 cm^{-1}), and δ(OCC)/δ(CCC) (◆; 490 cm^{-1}). The following parameters were used: energy of the electronic origin E (band 1, $E1$; band 2, $E2$); relative oscillator strength f (for the simulation only the ratio between band 1 and 2 is important, not the absolute magnitude); dimensionless displacements Δ which are given in terms of three d's for the three normal modes; and intrinsic line width Γ. For the fit of the absorption spectrum, the energies of the electronic origins have been shifted and the intensities of the two simulated bands have been scaled to the extinction coefficients obtained from the fit of the absorption data.

Scheme 1

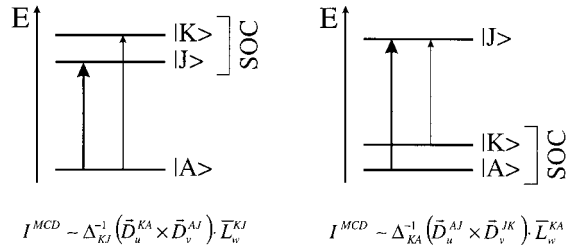

(88) In the case of the second mechanism in eq 1 (Scheme 1, right), the second transition dipole moment (in addition to $\vec{\mathrm{D}}_u^{AJ}$ for the transition from $|A\rangle$ to $|J\rangle$) corresponds to a virtual transition from the intermediate state $|K\rangle$ to $|J\rangle$, which usually is not observed spectroscopically.

left). If one alternatively considers the transition from $|A\rangle$ to $|K\rangle$, $|J\rangle$ becomes the intermediate state, and because of the sign change in the denominator Δ^{-1} that occurs when $|K\rangle$ and $|J\rangle$ are exchanged, the resulting **C** term signal changes sign. This corresponds to a pseudo-**A** term that is created by the spin−orbit coupling of excited states $|J\rangle$ and $|K\rangle$.

The resonance Raman data of **1** require the presence of a peroxide (π_v^*) to Fe(III) charge-transfer transition in the 600 nm region of the absorption spectrum. If one assumes that this CT state is one component of the pseude-**A** MCD signal, $|J\rangle$, then there are two possibilities for state $|K\rangle$: it can either be an overlap-forbidden charge-transfer transition from the in-plane peroxide π^* orbital (π_h^*, vide infra) or a ligand field (LF) excited state.[89] If $|K\rangle$ is this second alkylperoxo to Fe(III) CT state, however, both $|J\rangle$ and $|K\rangle$ have transition dipole moments that are oriented along the Fe−O bond. Therefore, the vector product ($\vec{D}_u^{KA} \times \vec{D}_v^{AJ}$) is zero and there is no MCD intensity. Alternatively, if $|K\rangle$ is identified with a LF excited state ($t_{2g} \rightarrow e_g$ transitions are located in this energy region as has been found for ls-[Fe(III)-BLM] and ls-[Fe(III)-BLM(OOH)] (ABLM)[13]), the spin−orbit coupling matrix element $\bar{L}_w^{KJ}$ is zero because the determinants representing $|J\rangle$ and $|K\rangle$ differ by two excitations, but $\boldsymbol{H}_{SOC}^w$ is a one-electron operator. The pseudo-**A** signal could formally be explained with both $|J\rangle$ and $|K\rangle$ being t_{2g} to e_g LF excited states, but related low-spin Fe(III) complexes (e.g. [Fe(III)-BLM] or ABLM[13]) do not show a pseudo-**A** MCD feature. In summary, the pseudo-**A** signal in the MCD spectrum of **1** cannot be explained with either of these two-state models.

The simultaneous fit of the absorption and MCD data together with the Heller analysis (vide infra) of the resonance Raman profiles provides strong evidence that the CT character of the 600 nm band is actually distributed over two states giving rise to the two intense absorption bands 1 and 2 in Figure 4. A mechanism for this observation could be strong configuration interaction (CI) mixing of the charge-transfer state with one of the ligand field states that are located in the 600 nm energy region. In Scheme 2, the Slater determinants of the ground state $|A\rangle$ and the CT state $|\Psi_1\rangle$ are diagramed together with one determinant that represents a ligand field state ($|\Psi_2\rangle$).[90] If we assume equal mixing of $|\Psi_1\rangle$ and $|\Psi_2\rangle$, two new states result:

$$|J_1\rangle = \frac{1}{\sqrt{2}}|\Psi_1 + \Psi_2\rangle$$

$$|J_2\rangle = \frac{1}{\sqrt{2}}|\Psi_1 - \Psi_2\rangle$$

By coupling both of these to a second ligand field state $|K\rangle$ as shown in Scheme 3 (a representative determinant of $|K\rangle$ is shown in Scheme 2), these two states give rise to a pseudo-**A** pattern. Starting from the first sum in eq 1 (cf. Scheme 1, left) and inserting $|J\rangle = 1/\sqrt{2}|\Psi_1 \pm \Psi_2\rangle$, one obtains:

$$I^{MCD} \sim \Delta_{KJ}^{-1}(\vec{D}_u^{KA} \times \vec{D}_v^{AJ})\cdot\bar{L}_w^{KJ} = \frac{1}{\Delta_{KJ}}\left[\langle K|u|A\rangle \times \frac{1}{\sqrt{2}}\langle A|v|\Psi_1 \pm \Psi_2\rangle\right]\cdot\frac{1}{\sqrt{2}}\langle K|\boldsymbol{H}_{SOC}|\Psi_1 \pm \Psi_2\rangle$$

Since $\langle K|\boldsymbol{H}_{SOC}|\Psi_1\rangle = 0$ (both determinants $|K\rangle$ and $|\Psi_1\rangle$ differ by more than one excitation), this expression reduces to

$$= \frac{1}{2\Delta_{KJ}}[\pm\langle K|u|A\rangle \times \langle A|v|\Psi_1\rangle \cdot\langle K|H_{SOC}|\Psi_2\rangle + \langle K|u|A\rangle \times \langle A|v|\Psi_2\rangle \cdot\langle K|H_{SOC}|\Psi_2\rangle] \quad (2)$$

In eq 2, the first term dominates because of the large transition dipole matrix element $\langle A|v|\Psi_1\rangle$ that corresponds to the CT transition. Experimentally, the lower energy transition has a positive sign and the higher energy feature a negative one. This means that the vector product $\langle K|u|A\rangle \times \langle A|v|\Psi_1\rangle\cdot\langle K|\boldsymbol{H}_{SOC}|\Psi_2\rangle$ is positive and the coefficient from the CI mixing then induces the observed sign change between the transitions from $|A\rangle$ to $|J_1\rangle$ (+ sign) and $|A\rangle$ to $|J_2\rangle$ (− sign), respectively, when $E_K > E_{J_1}, E_{J_2}$ (Scheme 3). For the third state $|K\rangle$, one obtains for the MCD intensity:

$$= \frac{1}{\Delta_{J_1K}}[\langle\Psi_1 + \Psi_2|u|A\rangle \times \langle A|v|K\rangle]\cdot\langle\Psi_1 + \Psi_2|\boldsymbol{H}_{SOC}|K\rangle + \frac{1}{\Delta_{J_2K}}[\langle\Psi_1 - \Psi_2|u|A\rangle \times \langle A|v|K\rangle]\cdot\langle\Psi_1 - \Psi_2|\boldsymbol{H}_{SOC}|K\rangle = \frac{\Delta_{J_2K} + \Delta_{J_1K}}{\Delta_{J_1K}\cdot\Delta_{J_2K}}[\langle\Psi_2|u|A\rangle \times \langle A|v|K\rangle\cdot\langle\Psi_2|\boldsymbol{H}_{SOC}|K\rangle] + \frac{\Delta_{J_2K} - \Delta_{J_1K}}{\Delta_{J_1K}\cdot\Delta_{J_2K}}[\langle\Psi_1|u|A\rangle \times \langle A|v|K\rangle\cdot\langle\Psi_2|\boldsymbol{H}_{SOC}|K\rangle]$$

taking into account that $\langle\Psi_1|\boldsymbol{H}_{SOC}|K\rangle = 0$. Since $|\Delta_{J_2K} + \Delta_{J_1K}/\Delta_{J_1K}\cdot\Delta_{J_2K}| \gg |\Delta_{J_2K} - \Delta_{J_1K}/\Delta_{J_1K}\cdot\Delta_{J_2K}|$, the second term in the above expression can be neglected. Using the relation $\Delta_{JK} = -\Delta_{KJ}$, one obtains for the MCD intensity of state $|K\rangle$:

$$\approx -\frac{\Delta_{KJ_2} + \Delta_{KJ_1}}{\Delta_{KJ_1}\cdot\Delta_{KJ_2}}[\langle\Psi_2|u|A\rangle \times \langle A|v|K\rangle\cdot\langle\Psi_2|\boldsymbol{H}_{SOC}|K\rangle] \quad (3)$$

This shows that the state $|K\rangle$ has less MCD intensity than the

Scheme 2

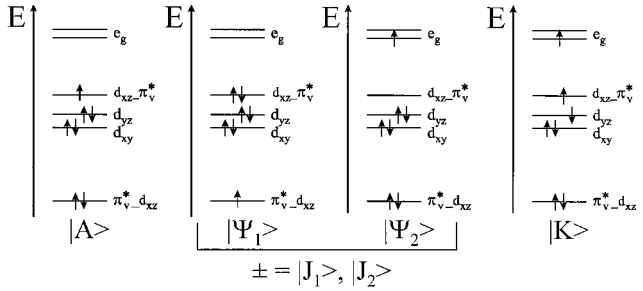

Scheme 3

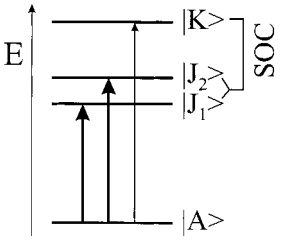

(89) Charge-transfer states from the other ligands of **1** (TPA and water or hydroxide) can be ruled out for $|K\rangle$. UV−vis absorption studies performed on the related iron(III) complex $[Fe(TPA)Cl_2]^+$ show that the charge-transfer transitions from the TPA ligand are below 350 nm.[55] In addition, absorption spectra of the active form of Soybean lipoxygenase which contains a high-spin Fe(III) −OH complex do not show hydroxide to Fe(III) charge-transfer transitions at wavelengths above 350 nm.[4]

pseudo-**A** from the two $|J\rangle$ states, because in eq 3 both transition dipole moments correspond to LF transitions whereas in eq 2 for transitions to $|J_1\rangle$ and $|J_2\rangle$, the larger dipole moment of the CT state contributes. In the MCD spectrum in Figure 4, negative band 3 can be associated with state $|K\rangle$.

In summary, the three-state model presented above (cf. Scheme 3) has several consequences for the UV−vis and MCD spectrum. The broad 600 nm absorption consists of a minimum of three bands: one alkylperoxo to Fe(III) CT state (from resonance Raman spectroscopy) that is CI mixed with a LF state. A second ligand field state spin−orbit couples to these two states creating the pseudo-**A** pattern in the MCD spectrum (cf. Scheme 3). Therefore, the 600 nm absorption feature has to be fit with two intense ($|J_i\rangle$) and one weak ($|K\rangle$) band as required by experiment in Figure 4. Because of the large transition dipole moment $\langle A|v|\Psi_1\rangle$ of the CT state, the pseudo-**A** signal has much more MCD intensity than the negative signal from state $|K\rangle$.

(b) Heller Analysis of the Resonance Raman Profiles. Further support for the assignment of bands 1 and 2 to an alkylperoxo to Fe(III) charge-transfer state mixed with a d−d transition can be obtained from a Heller analysis of the resonance Raman profiles in terms of excited-state distortions.[65−68] Figure 5 (bottom) shows the three resonance profiles of the ν(OO), ν(FeO), and δ(OCC)/δ(CCC) vibrations. The shapes of these profiles are clearly asymmetric which cannot be reproduced when simulated with only one excited state. Using a model with two excited states that have CT contributions, the fit obtained for the profiles resembles the halfwidths and the shapes of the experimental data well. Importantly, the fit of the shapes of the profiles imposes important restrictions both on the energetic separation of the two states and on the ratio of their displacements. From the Heller simulation, the two transitions with CT character are separated by about 1300 cm^{-1}, which was used as a further restriction to fit the absorption and MCD spectra (vide supra). Furthermore, both transitions have about the same dimensionless displacements Δ which means that the CT character is about equally distributed over the two states. This is in agreement with the interpretation of the pseudo-**A** term MCD signal (vide supra). Figure 5 (bottom) shows the Heller fits of the profiles together with the fit parameters. The electronic origin of band 1 is at 13 100 cm^{-1} and the dimensionless displacements for the different normal modes are $\Delta1(O-O) = -0.97$, $\Delta1(Fe-O) = +1.81$, and $\Delta1(bend) = +0.65\cdot\Delta1(Fe-O)$. Note that the Heller analysis does not give the sign of Δ; this information is obtained from the assignment of the CT transition (cf. Section B). Since the 490 cm^{-1} bending vibration gains its intensity by mixing with ν(FeO), the displacement of this mode is related to $\Delta1(Fe-O)$. The coefficient of 0.65 corresponds to an admixture of about 39% ν(FeO) into δ(OCC)/δ(CCC) and is in agreement with the estimated coefficient of 0.55−0.60 calculated with the preresonance formula:[68,91,92]

$$\frac{I(\mathrm{Fe-O})}{I(\mathrm{bend})} = \left(\frac{\Delta(\mathrm{Fe-O})\cdot\nu(\mathrm{FeO})}{\Delta(\mathrm{bend})\cdot\nu(\mathrm{bend})}\right)^2 \qquad (4)$$

where I is the integrated resonance Raman peak intensity at a specific excitation wavelength and v is the vibrational energy. The electronic origin of band 2 is at 13 900 cm^{-1}. This transition has slightly larger displacements than band 1 ($\Delta2 = 1.18\cdot\Delta1$) which is in agreement with the fit of the absorption spectrum where band 2 has more intensity than band 1 (cf. Figure 5, top). This indicates that band 2 actually has more CT character than band 1. However, the intensity ratio of these bands from the fit of the absorption and MCD spectra (about 1.4) as well as from the Heller fit (about 1.2) has some flexibility and cannot be determined with high accuracy. Figure 5 (top) shows the experimental absorption spectrum together with the fitted bands 1 and 2 (dashed lines; cf. Figure 4, top) and the corresponding Heller simulation of the absorption bands 1 and 2 (solid line) which shows good agreement. The same set of parameters has been used for the Heller simulation of the resonance Raman profiles and the absorption bands with the exception of the energies of the electronic origins[93] $E1$ and $E2$ which shift by about 1000 cm^{-1} due to the different experimental conditions (solution (−40 °C) vs frozen solution (77 K); cf. Experimental Section).

From the dimensionless displacements Δ, the Huang−Rhys parameter S_p^J for excited state $|J\rangle$ and normal mode p can be calculated: $S_p^J = {}^1/_2(\Delta_p^J)^2$. Absolute displacements along the internal coordinate i (in Å) can be obtained with the formula:[67]

$$\Delta r_i(\text{Å}) = 5.8065\sum_p l_{p,i}\frac{\Delta_p}{\sqrt{\nu_p}} \qquad (5)$$

with $l_{p,i}$ being the eigenvector from NCA for normal mode p, Δ_p is its dimensionless displacement and υ_p is the vibrational energy (in cm^{-1}). For bond distances, the eigenvector $l_{p,i}$ is directly related to the change in bond length, hence eq 5 gives the absolute displacement along the bond. Table 4 lists the distortions calculated with eq 5 for bands 1 and 2 from the Heller analysis using the eigenvectors from QCA-NCA. No accurate description with NCA has been obtained for the bending vibration at 490 cm^{-1} (vide supra), which is therefore not included in Table 4. This mode has a significant displacement along the Fe−O stretching coordinate, hence the total displacement in this direction can be expected to be larger than listed in Table 4. The distortions along the Fe−O−O and C−O−O angle bending coordinates calculated with eq 5 are obtained in angstroms. Applying the method described in the Appendix, the distortions along the bends are transformed into grad units. As can be seen from Table 4, the angular distortions obtained are very small.

Since absorption bands 1 and 2 gain intensity from the CT contribution, adding up their distortions should give the total displacement of the CT state relative to the ground state. However, the total distortion of bands 1 and 2 along the Fe−O bond (+0.24 Å) is too large compared to the low donor strength (vide infra) of the CT transition. Importantly, the LF states in this energy region involve t_{2g} to e_g excitations and also have large distortions along metal−ligand bonds even though their extinction coefficients are low. Therefore, the total Fe−O distortion given in Table 4 reflects the CI mixing of the CT state with a LF state which both contribute with their individual distortions. Spectroscopically, the CI mixing of the CT and LF

(90) In general, the ligand field states corresponding to the t_{2g} to e_g excitations are linear combinations of several Slater determinants. Since the analysis presented here does not require a specific assignment of the d−d transition, single determinants are sufficient to develop the three-state pseudo-**A** model.

(91) Tang, J.; Albrecht, A. C.; Szymanski, H. A., Eds. Plenum Press: New York, 1970; Vol. 2, pp 33−68.

(92) Warshel, A.; Dauber, P. *J. Chem. Phys* **1977**, *66*, 5477.

(93) In Heller theory, the displacement parameters Δ determine the shapes of the Raman profiles and absorption bands as well as the shifts of their maxima relative to the energies of the electronic origins. However, the energetic difference between the Raman profile and absorption band maxima does not vary much with the Δ values. Therefore, the relative shifts of the electronic origins in the two fits cannot be compensated without strongly affecting the shapes of the Raman profiles and absorption bands.

Table 4. Excited State Distortions Calculated from the Simultaneous Heller Fit of the Resonance Raman Profiles and Absorption Bands 1 and 2

	ν (cm^{-1})	ΔFe−O [Å]	ΔO−O [Å]	ΔC−O [Å]	∠FeOO [Å]	∠COO [Å]	∠FeOO [deg]	∠COO [deg]
*E*1	796	+0.0164	−0.0685	+0.0269	+0.0108	+0.0155	+0.2	+0.4
	696	+0.0938	+0.0015	−0.0544	-0.0364	-0.0483	-0.8	−1.7
	490[a]							
*E*2	796	+0.0193	−0.0809	+0.0317	+0.0127	+0.0183	+0.3	+0.5
	696	+0.1106	+0.0018	−0.0642	−0.0430	−0.0567	−0.9	-2.0
	490[a]							
*E*1 + *E*2	796	+0.0357	−0.1494	+0.0586	+0.0235	+0.0338	+0.5	+0.9
	696	+0.2044	+0.0033	−0.1186	−0.0794	−0.1050	−1.7	−3.7
	490[a]							
total		+0.2401	−0.1461	−0.0600	−0.0559	−0.0712	−1.2	−2.8

[a] Value not accessible since NCA does not provide a reasonable fit for this mode.

Table 5. Comparison of Relative Donor Strengths and M−O Force Constants of Cu− and Fe−Peroxo Complexes

complex	$\pi^* \rightarrow$ d CT (cm^{-1})	donor strength $(C^M_{\pi^*})^2$ ratio [a]	ν_{M-O} (cm^{-1})	k_{M-O} (mdyn/Å)[b]	ν_{O-O} (cm^{-1})	k_{O-O} (mdyn/Å)[b]	ref
Cu end-on monomer	19880	1.0	488	1.94 (1.89)	803	2.90 (2.86)	117
Cu end-on dimer	19085	1.9	561	1.99 (1.94)	832	3.17 (3.10)	118
Cu side-on dimer	26570	3.7	572	1.54 (1.42)	763	2.43 (2.43)	95
Fe(III) end-on dimer	14620 24650 26200	1.4−1.8	421	1.99	876	3.07	69
L3CuOOCm[d]	16590	1.1	645	3.03	843/809	3.22	94
L3CuOOH	16560	>0.3	624	2.94	843	3.51	
side-on hs-Fe(EDTA)O_2	18800 21700 25250 31050	0.7−1.2	459	1.56	816	3.02	119
ls-Fe(TPA)OO^{t}Bu	16000 17364	0.5	696	3.53	796	2.92	*c*

[a] Corresponds to the charge donation of peroxide to the metal relative to the end-on monomer (set to 1.0). [b] Urey−Bradley force constants in parentheses, cf. ref 94. [c] This work. [d] Cm = Cumene.

state is directly reflected in the MCD pseudo-**A** signal (vide supra). The total distortion along the O−O bond (−0.14 Å) is reasonable for a CT state.[69,94]

A.3. Donor Strength of the Charge-Transfer State. The above analysis of the UV−vis, MCD, and resonance Raman data shows that both bands 1 and 2 gain their intensity from an alkylperoxo to Fe(III) charge-transfer transition. Assuming that the contribution to the intensity from the CI mixed LF state (vide supra) is small, the oscillator strengths of bands 1 and 2 (Table 3) can be used to estimate the relative donor strength of the alkylperoxo ligand orbital π^*_v corresponding to this CT transition. Using the formalism of Baldwin et al.,[95] the donor strength of a ligand is approximately given by:

$$(C^M_{\pi^*})^2 = 9.22 \times 10^{-2}[\text{Å}] \times \sum_i \frac{f_i}{\nu_i |\mathbf{r}|^2}$$

with f being the oscillator strength and υ the frequency of the ith charge-transfer band and **r** the transition vector that coincides with the Fe−O bond and which can be set to the Fe−O bond length. This equation relates the metal d orbital contributions to the ligand donor orbitals and therefore the strength of the metal−ligand bond to the intensity of the resulting CT transition. The donor strength is calibrated relative to the value obtained for an end-on Cu−peroxide monomer whose donor strength has been set to 1.0. For complex **1**, a low value of 0.5 is calculated for combined bands 1 and 2 corresponding to the alkylperoxo (π^*_v) to Fe(III) CT transition. Table 5 contains the relative donor strengths of a series of compounds. Most useful is the comparison between **1** and the Cu−alkylperoxo complex [(L3)-Cu(OOCm)], which has a *larger* relative donor strength of 1.1 than **1** but a *smaller* metal−O force constant. This is a clear indication that in addition to the Fe−OO^{t}Bu π^*_v bonding interaction reflected by the 600 nm CT transition, there must be other Fe(III)−OO^{t}Bu bonding interactions in **1** that contribute to the strong Fe−O bond.

B. Density Functional Calculations. The analysis of the spectroscopic data has shown that there is a CT transition in the 600 nm region of the absorption spectrum of **1** that is distributed over two bands. The mechanism for this distribution is a CI mixing of the CT state with a LF state which is manifested in a pseudo-**A** MCD signal, the shapes of the resonance Raman profiles, and the large distortions obtained from the Heller fit. The relative donor strength of the corresponding Fe−O bond of 0.5 is low, which is in contrast to the large Fe−O force constant corresponding to a strong Fe−O bond. But whereas the metal−ligand force constant contains contributions to the metal−ligand bond from all the different valence orbital interactions, the relative donor strength observed experimentally for the 600 nm absorption is a selective measure of the strength of the π^*_v orbital interaction. This is a clear indication that for **1** there must be additional contributions to the Fe−O bond. To gain further inside into the nature of the 600 nm CT state and to identify these additional contributions

(94) Chen, P.; Fujisawa, K.; Solomon, E. I. *J. Am. Chem. Soc.* **2000**, *122*, 10177

(95) Baldwin, M. J.; Root, D. E.; Pate, J. E.; Fujisawa, K.; Kitajima, N.; Solomon, E. I. *J. Am. Chem. Soc.* **1992**, *114*, 10421.

Table 6. Calculated (B3LYP/LanL2DZ) Geometries and Properties of Three Models for Low-spin $[Fe(TPA)(OH_x)(OO^tBu)]^{x+}$ (1)

	geometric parameters [a]						
molecule	r(Fe−O)	r(O−O)	r(C−O)	r(Fe−OH_x)	r(Fe−N)[b]	∠FeOO	∠COO
ls-$[Fe(NH_3)_4(OH_2)(OO^tBu)]^{2+}$ (**$\tilde{1}$**)	1.818	1.488	1.565	2.024	2.045	111	112
ls-$[Fe(NH_3)_4(OH)(OO^tBu)]^{+}$ (**$\tilde{1}$a**)	1.835	1.505	1.510	1.884	2.054	111	110
ls-$[Fe(Ime)_3(NH_3)(OH_2)(OO^tBu)]^{2+}$ [e]	1.825	1.483	1.552	2.014	2.007[c]	112	112

	Mulliken charges						spin densities				
molecule	Fe	O2	O3	C_{3t}	ΣOOR	$O(H_x)$[d]	Fe	O2	O3	C_{3t}	$O(H_x)$[d]
ls-$[Fe(NH_3)_4(OH_2)(OO^tBu)]^{2+}$ (**$\tilde{1}$**)	+0.51	−0.29	−0.33	+0.36	−0.12	−0.74	+0.77	+0.24	+0.05	0	0
ls-$[Fe(NH_3)_4(OH)(OO^tBu)]^{+}$ (**$\tilde{1}$a**)	+0.43	−0.36	−0.30	+0.40	−0.30	−0.71	+0.95	+0.11	+0.01	0	−0.02
ls-$[Fe(Ime)_3(NH_3)(OH_2)(OO^tBu)]^{2+}$ [e]	+0.50	−0.29	−0.30	+0.37	−0.12	-0.69	+0.73	+0.26	+0.06	0	−0.01

[a] Bond lengths in Å. [b] Averaged over all Fe−N bonds. [c] For the model with three imines, the average Fe−N_{IM} bond length is 2.001 Å, and the remaining Fe−N_{AM} is 2.023 Å. [d] Charge and spin density on the oxygen of the water or hydroxo ligand, respectively. [e] Ime = imine ligand H−N=CH_2 as a model for pyridine.

Table 7. Calculated (B3LYP/LanL2DZ) and Experimental Frequencies and Force Constants

	force constant (mdyn/Å)			frequency (cm^{-1})	
calculated/**experimental**	Fe−O	O−O	C−O	Fe−O	O−O
calc: HOOH		4.40			905
NCA: HOOH[a]		**4.01**			**880**
calc: HOO^-		3.08			750
exp: HOO^-[b]					**775**
calc: $^-O-O^-$		1.94			641
calc: ^{t}BuOOH		3.92	3.81		900
exp: ^{t}BuOOH−NCA: CH_3OOCH_3 [c]		**4.07**	**4.56**		**884 (?)**
calc: ^{t}BuOO$^-$		3.13	4.46		810
calc: ls-$[Fe(NH_3)_4(OH_2)(OO^tBu)]^{2+}$ (**$\tilde{1}$**)	3.38	3.39	2.43	626	843
calc: ls-$[Fe(NH_3)_4(OH)(OO^tBu)]^{+}$ (**$\tilde{1}$a**)	2.89	3.47	3.46	625[d]	877
calc: ls-$[Fe(Im)_3(NH_3)(OH_2)(OO^tBu)]^{2+}$	3.13	3.38	2.63	630	815
NCA: ls-$[Fe(TPA)(OH_x)(OO^tBu)]^{x+}$	**3.53**	**2.92**	**2.83**	**696**	**796**

[a] Measured in the gas phase.[120] [b] Determined with photoelectron spectroscopy in the gas phase;[121] the error of this value is ±250 cm^{-1}. Calculations (GVB−CI) lead to values of 777−820 cm^{-1} for ν(OO). [c] The IR spectrum (gas phase) of ^{t}BuOOH in ref 122 has not been assigned; the O−O and C−O force constants have been calculated for CH_3OOCH_3[123] where ν(OO) = 779 cm^{-1} (see text). [d] Raised in energy by interaction with the Fe−OH stretch (ν(Fe−OH) = 575 cm^{-1}; k = 2.623 mdyn/Å).

to the Fe−O bond, density functional (DFT) calculations have been performed.

The crystral structure of **1** is not known and the sixth ligand could either be water or hydroxide. To determine a reasonable structure for **1**, two possible model systems, low-spin $[Fe(NH_3)_4(OH_2)(OO^tBu)]^{2+}$ (**$\tilde{1}$**) and low-spin $[Fe(NH_3)_4(OH)(OO^tBu)]^{+}$ (**$\tilde{1}$a**), have been fully geometry optimized and evaluated based on the spectroscopic data.

B.1. Geometry and Evaluation based on Calculated Spectral Features. Table 6 compares the calculated structures for **$\tilde{1}$** (Figure 3) and **$\tilde{1}$a** (Supporting Information, Figure 1). Since water is a worse donor than hydroxide, the remaining ligands (especially alkylperoxide) donate more charge to Fe(III) in the case of **$\tilde{1}$**, which is manifested in shorter Fe−L (L = OO^tBu, NH_3) bond lengths compared to **$\tilde{1}$a**. The structural parameters of **$\tilde{1}$** are consistent with the crystal structure of [Cu(L_1)(OOCm)], where r(Cu−O) = 1.816 Å, r(O−O) = 1.460 Å, and r(C−O) = 1.457 Å.[51] Nevertheless, this comparison has limited significance since it involves Cu(II) rather than low-spin Fe(III). A better comparison between the model systems is provided by the calculated force fields which are a direct reflection of the electronic structure. Table 7 shows the calculated frequencies and force constants of **$\tilde{1}$** and **$\tilde{1}$a** in comparison to the experimental (QCA-NCA) values. Importantly, while both model systems do not accurately reproduce the spectroscopic results of a strong Fe−O (k = 3.53 mdyn/Å) and weak O−O (k = 2.92 mdyn/Å) bond, for **$\tilde{1}$** both force constants have about the same magnitude ($k \approx$ 3.4 mdyn/Å), whereas for **$\tilde{1}$a** the calculated trend is reversed from experiment with the Fe−O being weaker (k = 2.89 mdyn/Å) than the O−O bond (k = 3.47 mdyn/Å). This is due to the better donor capability of the hydroxo ligand in **$\tilde{1}$a** which leads to less donation from the ^{t}BuOO$^-$ group. These results strongly indicate that the electronic structure of model system **$\tilde{1}$** better resembles the situation in complex **1**.

Both **$\tilde{1}$** and **$\tilde{1}$a** have four NH_3 donors replacing the TPA ligand of **1**. To test the validity of this approximation, a model system was constructed where starting from **$\tilde{1}$**, three of the ammonias have been substituted by imines (Ime; H−N=CH_2), which better model the pyridine donors in the TPA ligand (cf. Supporting Information, Figure 1). The calculated bond lengths, charges, spin densities, and vibrational properties of this system (fully optimized) closely resemble the results obtained for **$\tilde{1}$** (cf. Tables 6 and 7), which shows that ammonias are reasonable approximations for pyridines in electronic structure calculations.[96]

Thus, model **$\tilde{1}$** is supported by the spectroscopic results and will be used to analyze the electronic structure of **1**. The thermodynamics of the homolytic cleavage reaction[58,59] have been calculated for both **$\tilde{1}$** and **$\tilde{1}$a** to account for the possible change in protonation on oxidation (vide infra).

B.2. Description of the Electronic Structure of 1. The spin-unrestricted molecular orbital diagram of complex **1** (calculated for **$\tilde{1}$** using the B88P86 functional and a Slater-type triple-ζ (valence) basis set; see Experimental Section) is shown in Figure

(96) The imines give rise to shorter Fe−N bond lengths (2.00 Å average; cf. Table 6) which reflect the fact that H−N=CH_2 is a weaker σ donor than NH_3. Since this decreased donor strength is compensated by the shorter bond distances, the extended model system does not offer improved results for the Fe(III)−alkylperoxo bond. Experimentally, the low-spin complex $[Fe^{III}(5\text{-}Me_3TPA)(acac)]^{2+}$ [32] has an average Fe−N distance of 1.96 Å, which is in agreement with the calculation.

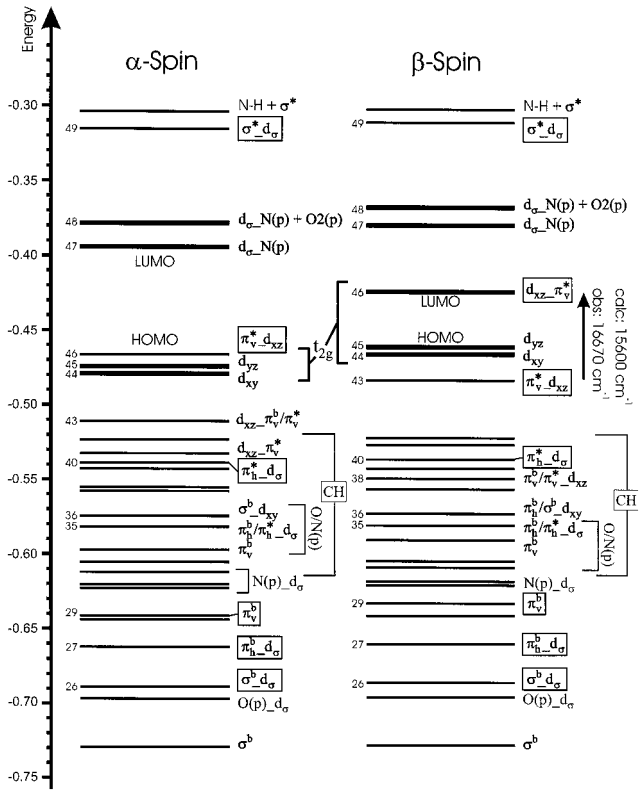

Figure 6. Molecular orbital diagram of **1̃** (the structure of which is shown in Figure 3 together with the applied coordinate system) calculated with the B88P86/triple-ζ basis. The orbitals of the alkylperoxo ligand are labeled as shown in Figure 1. The nomenclature "*a*_*b*" is used for Fe and ^{t}BuOO$^-$ MOs and indicates that orbital *a* interacts with *b* and that *a* has a larger contribution to the resulting MO. Important MOs corresponding to the donor orbitals of the alkylperoxo ligand are marked with a box. For β-spin-orbitals included in Table 8 and the corresponding α-spin-orbitals, the continuous MO numbers (as they appear in the calculation) are given on the left side of the horizontal lines. Thick lines correspond to MOs with large iron d contributions (>50%).

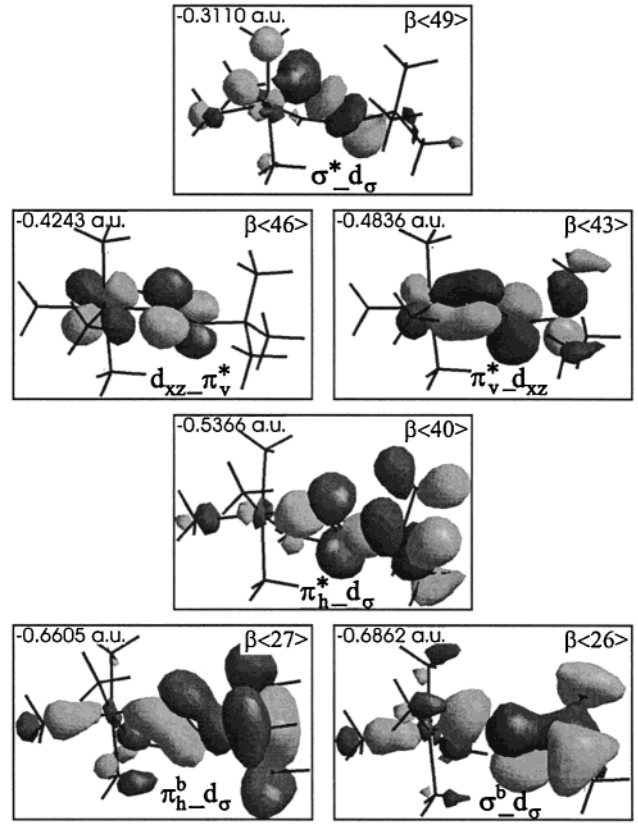

Figure 7. Contour plots of the molecular orbitals of **1̃** (cf. Figure 6 and Table 8) corresponding to the most important interactions of the alkylperoxo donor (π^*_v, π^*_h, π^b_h, and σ^b) and acceptor (σ^*) orbitals with the d functions of iron(III).

6. In an octahedral environment, the five d orbitals of iron are split into a 3-fold degenerate t_{2g} (d_{xy}, d_{yz}, d_{xz}) and a 2-fold degenerate e_g set (d_{z^2}, $d_{x^2-y^2}$), where the t_{2g} orbitals mediate π interactions with the ligands and the e_g orbitals form σ bonds. In the case of low-spin iron(III), the t_{2g} orbitals are occupied by five electrons and the e_g orbitals are empty (ground-state electron configuration). In a spin-unrestricted scheme, this is equivalent to having all three α t_{2g} orbitals occupied and one orbital unoccupied in the β t_{2g} set (the LUMO). The ^{t}BuOO$^-$ ligand has low-lying π and σ donor orbitals but no accessible acceptor MO, hence this ligand forms donor bonds with empty d orbitals of Fe(III). Since there is only one unoccupied t_{2g} function available (in the coordinate system shown in Figure 3 this is the β-d_{xz} LUMO), only the β-spin MOs will contribute to π bonding. The e_g set is unoccupied such that both α- and β-spin MOs participate in σ bonding. Since the spin-polarization effect on the d orbitals is small,[97] σ bonding is almost identical for the α and β set and the corresponding α and β MOs are very similar. This leads to the overall similar appearance of the α- and β-spin MO diagrams in Figure 6. Therefore, the β-spin MOs will be analyzed below.

The HOMO of the ^{t}BuOO$^-$ ligand, π^*_v, acts as a π donor and interacts with the β-d_{xz} orbital of iron(III) which represents the hole in the t_{2g} set as described above. The resulting π bond is manifested in the bonding combination of these orbitals, π^*_v_d_{xz} ($\beta\langle 43\rangle$),[98] as shown in Figure 7. The corresponding antibonding combination, d_{xz}_π^*_v ($\beta\langle 46\rangle$), is the LUMO of complex **1**. The orbital π^*_v_d_{xz} has about 30% metal character (cf. Table 8), which indicates that this π bond is very strong. This is also reflected by the large shift of the β antibonding orbital d_{xz}_π^*_v to higher energy compared to the other t_{2g} orbitals (d_{yz} and d_{xy}) in Figure 6, right. In addition, since occupied α and β spin functions are similar for the σ bonding MOs (vide supra), the net spin density is a very sensitive probe of the strength of the π bond. As shown in Table 6, there is no appreciable spin density on the water/hydroxo ligand, which means that indeed the hole in the t_{2g} set points toward the alkylperoxo group. The total spin density on the ^{t}BuOO$^-$ ligand of +0.29 for **1̃** (from the B3LYP/LanL2DZ calculation, cf. Table 6) again indicates a strong interaction.[99] The calculated excitation energy (ΔSCF performed with ADF) for the transition from π^*_v_d_{xz} to d_{xz}_π^*_v is 15 600 cm^{-1}, which is in good agreement with the observed charge-transfer band in the absorption spectrum that is centered around 16 670 cm^{-1}. This together with the spectroscopic data allows the assignment of the 600 nm CT absorption feature as the π^*_v_d_{xz} to d_{xz}_π^*_v transition associated with the Fe−O π bond. However, the calculated large

(97) For low-spin Fe(III), the difference of the number of α and β d electrons is α − β = 1. This is in contrast to high-spin iron(III) where α − β d electrons = 5. In this case, bonding is very different in the α and β MOs.

(98) Regarding the nomenclature: "π^*_v_d_{xz}" denotes an MO that is a mixture of the orbitals π^*_v and d_{xz}; the one with the larger contribution to the MO comes first (in this example π^*_v). $\beta\langle 43\rangle$ refers to MO #43 with β spin.

(99) For model **1̃a** with the hydroxo ligand, the alkylperoxide carries a spin density of +0.12 (cf. Table 6). This indicates that the model with the water ligand (**1̃**) has a distinctly stronger π bond than **1̃a**.

Table 8. Charge Contributions of Important β Orbitals of $\tilde{\mathbf{1}}$ Calculated with the B88P86/Triple-ζ Basis

no.	label	energy (hartree)	Fe	O2		O3		C_{3t}	O8	ΣN
			d	s	p	s	p	s+p	s+p	s+p
$\beta\langle 49\rangle$	σ^*_d_σ	−0.3110	3	2	25	2	25	1	0	3
$\beta\langle 48\rangle$	d_σ_N(p) + O2(p)[a]	−0.3679	62	1	11	0	2	1	0	17
$\beta\langle 47\rangle$	d_σ_N(p)	−0.3799	71	0	1	0	0	0	4	16
$\beta\langle 46\rangle$	d_{xz}_π_v^* (LUMO)	−0.4243	60	0	26	0	10	0	0	0
$\beta\langle 45\rangle$	d_{yz} (HOMO)	−0.4612	92	0	0	0	0	0	3	0
$\beta\langle 44\rangle$	d_{xy}	−0.4638	89	1	1	0	4	0	0	0
$\beta\langle 43\rangle$	π_v^*_d_{xz}	−0.4836	30	0	13	0	39	2	0	0
$\beta\langle 40\rangle$	π_h^*_d_σ[a]	−0.5366	3	0	19	0	25	4	1	3
$\beta\langle 38\rangle$	π_v^b/π_v^*_d_{xz}	−0.5495	2	0	11	0	2	1	0	1
$\beta\langle 36\rangle$	π_h^b/σ^b_d_{xy}	−0.5730	2	0	21	1	3	2	7	11
$\beta\langle 35\rangle$	π_h^b/π_h^*_d_σ[a]	−0.5809	2	0	11	0	0	1	42	23
$\beta\langle 29\rangle$	π_v^b	−0.6330	1	0	11	0	24	14	1	4
$\beta\langle 27\rangle$	π_h^b_d_σ[a]	−0.6605	3	1	14	0	13	16	2	8
$\beta\langle 26\rangle$	σ^b_d_σ[a]	−0.6862	4	0	22	3	24	7	2	8

[a] The charge contributions are the average of α and β orbitals (both are very similar) to illustrate σ bonding.

covalency of this bond is not in agreement with the low donor strength and small extinction coefficient of the corresponding absorption band, indicating that the calculation overestimates this covalency. This can be quantified by comparison with a Cu(II)−alkylperoxo complex ([(L3)Cu(OOCm)], cf. Table 5) that has a relative donor strength of about 1.0 (ϵ = 5400 $M^{-1}cm^{-1}$) for the corresponding π bond between π_v^* and $d_{x^2-y^2}$ of copper(II). For this complex, the covalency could be determined experimentally (from EPR spectroscopy) to be 38%.[94] In the spin-unrestricted formalism, this can be interpreted in the sense that the β−$d_{x^2-y^2}$ function of Cu(II) has a total admixture of ligand donor orbitals of 38% corresponding to a metal contribution of 62%. In comparison, d_{xz}_π_v^* has about 36% π_v^* character (cf. Table 8), hence the calculated π covalency for $\tilde{\mathbf{1}}$ is comparable to that of the Cu(II) complex. However, the experimental donor strength of **1** is only 0.5 (cf. Table 5). Thus, the π_v^* covalency of **1** must be lower than calculated for $\tilde{\mathbf{1}}$ and can be estimated from its CT intensity to be about 20%. In the B3LYP/LanL2DZ calculation of $\tilde{\mathbf{1}}$, the π_v^* covalency is also overestimated at ∼30% (data not shown).

All the spectroscopic methods applied to **1** (vide supra) monitor this π bond between iron(III) and the alkylperoxo ligand with the exception of the Fe−O force constant (obtained from the vibrational data) which is a measure of the total bonding. However, as determined above, the large Fe−O force constant of 3.53 mdyn/Å is not in agreement with the observed donor strength of the π bond. Therefore, additional bonding interaction(s) between iron and the ^{t}BuOO$^-$ ligand must be present in **1**. Since π_v^b does not mix much with the iron d orbitals (cf. Table 8; $\beta\langle 29\rangle$), these additional contributions must be of σ type. The three available σ donor orbitals π_h^*, π_h^b, and σ^b interact with one of the e_g type functions (which are denoted "d_σ" since d_{z^2} and $d_{x^2-y^2}$ are mixed). Each of the resulting bonding MOs, π_h^*_d_σ ($\beta\langle 40\rangle$), π_h^b_d_σ ($\beta\langle 27\rangle$), and σ^b_d_σ ($\beta\langle 26\rangle$) (cf. Figure 7), has about 3 to 4% metal character. Although the total σ covalency is small compared to the highly covalent π bond, these have to be doubled to account for contributions from both α- and β-spin orbitals (i.e. the e_g set is unoccupied in ls d^5). In addition, levels that are further away in energy contribute more to the bond strength for the same mixing coefficient. The e_g orbital $\beta\langle 48\rangle$ is directed toward the alkylperoxo ligand and has about 15% contribution from the ^{t}BuOO$^-$ ligand (mainly localized on O2), which sums up the σ interactions with the different donor orbitals. The overall strong Fe(III)−OO^{t}Bu σ interaction leads to the observed large Fe−O force constant corresponding to a strong Fe−O bond. No experimental absorption bands can be identified with the Fe−O σ bond. The energies of CT transitions can be estimated from the orbital energy differences[100] Δe. The first actual σ transition from π_h^*_d_σ to d_σ_N(p) ($\beta\langle 48\rangle$) has Δe = 37020 cm^{-1} (270 nm), which is far in the UV region. Thus, for the low-spin ferric complex **1** the Fe−O σ bonding interaction is not experimentally accessible with absorption, MCD, and resonance Raman spectroscopies.

The three σ donor orbitals π_h^*, π_h^b, and σ^b of the alkylperoxo ligand interact with Fe(III) as described above. Importantly, the main contributions to the Fe−O σ bond emerge from the O−O and C−O *bonding* orbitals π_h^b and σ^b. Donation out of these orbitals will therefore weaken the O−O and C−O bonds. Hence, the smaller O−O (2.92 mdyn/Å) and C−O (2.83 mdyn/Å) force constants of **1** compared to the free ^{t}BuOO$^-$ ligand (k_{O-O} = 3.13 mdyn/Å and k_{C-O} = 4.46 mdyn/Å; cf. Table 7) are a direct reflection of the strong σ interaction between iron(III) and alkylperoxide. Note that while the O−O force constant also has a contribution from the π interaction (donation out of π_v^* will partially strengthen this bond), the C−O force constant is only dependent on the σ donor interaction and therefore serves as a probe for σ bonding. This can be used to understand the trend in the force constants between $\tilde{\mathbf{1}}$ and $\tilde{\mathbf{1}}$**a** in Table 7.[101] Experimentally, the Fe−O is larger than the O−O force constant which is in contrast to $\tilde{\mathbf{1}}$ where both are of the same magnitude (cf. Table 7). Since the experimental data indicate that the π covalency is overestimated in the calculations of $\tilde{\mathbf{1}}$ (vide supra), the calculated σ interaction appears to be underestimated: using the force constants of $\tilde{\mathbf{1}}$ as a starting point and extrapolating their changes upon weakening of the π bond and strengthening of the σ interaction leads to a minor change of the Fe−O bond strength but a distinct weakening of the O−O bond in agreement with the experimental force constants.

Another possible mechanism to reduce the O−O force constant would be a strong back-bonding interaction between the O−O antibonding orbital σ^* and an occupied t_{2g} function of iron. Although σ^* is low in energy because of interaction with the *tert*-butyl group attached to oxygen and the long O−O bond distance, there is little evidence for such an interaction in the calculations. In fact, σ^* mainly mixes with one of the iron e_g orbitals. The resulting antibonding combination, σ^*_d_σ ($\beta\langle 49\rangle$), is shown in Figure 7 and has about 3% metal contribution. Since the e_g orbitals are unoccupied, this interaction does not contribute to bonding. Note that although σ^* does not participate in bonding, it is low in energy and activated for electrophilic reaction.

B.3. Thermodynamics of the Homolytic Cleavage of the O−O Bond. The low-spin Fe(III)−OO^{t}Bu complex **1** has been shown to undergo homolytic cleavage of the O−O bond forming an iron(IV)−oxo intermediate and an alkoxy radical[58,59] (see

(100) For the π bond, for example, Δe = 13010 cm^{-1} compared to 15600 cm^{-1} calculated for the transition from π_v^*_d_{xz} to d_{xz}_π_v^*. Next in energy is the CT transition from π_h^*_d_σ to d_{xz}_π_v^* with Δe = 24650 cm^{-1}, which, however, is overlap forbidden and does not have much intensity.

(101) Complexes $\tilde{\mathbf{1}}$ and $\tilde{\mathbf{1}}$**a** (cf. Table 7) show an interesting trend where $\tilde{\mathbf{1}}$ has a stronger Fe−O and weaker C−O force constant than $\tilde{\mathbf{1}}$**a**, but both have about the same O−O bond strength. The magnitude of the C−O force constant clearly indicates that $\tilde{\mathbf{1}}$ has a stronger σ bond than $\tilde{\mathbf{1}}$**a**. Combined with the stronger π bond in $\tilde{\mathbf{1}}$ (from the spin densities, vide supra), this explains why the Fe−O force constant of $\tilde{\mathbf{1}}$ is larger. The increased π donation in $\tilde{\mathbf{1}}$ should also lead to a strengthening of the O−O bond, but this is compensated by the increased σ interaction that weakens the O−O bond. Both effects cancel leaving the O−O force constant almost unchanged.

Table 9. Thermodynamics of the Homolytic Cleavage of the O−O Bond in **1̃a** and **1̃** (calculated with B3LYP)

		Δ*E* (kcal/mol)		Δ*E* (kcal/mol)[b]		Δ*E* (kcal/mol)[b]			
reactant	product[a]	LanL2	+ Solv[d]	TZV	+ Solv[d]	TZV+	+ Solv[d]	−*T*·DS (kcal/mol)	ZPCE (kcal/mol)
1̃a ($S = {}^1/_2$)	$S = 0$	56.7	47.4	51.2	41.9	50.4	40.6	−12.2	−2.5
	$S = 1$	30.3	21.7	24.8	16.0	23.9	14.6	−13.2	−2.6
	$S = 2$[c]	32.3	25.6	23.6	16.7	22.6	15.0	−15.8	−4.4

		Δ*E* (kca/mol)		Δ*E* (kca/mol)[b]	
reactant	product[a]	LanL2	+ Solv[d]	TZV	+ Solv[d]
1̃ ($S = {}^1/_2$)	$S = 1$	48.7	28.4	42.5	22.0
	$S = 2$[c]	50.6	33.8	41.0	23.9

[a] Spin state of the Fe(IV)═O complex; the ·OR radical has $S' = {}^1/_2$. Total spin: $S_{tot} = S \pm S'$. [b] Shifts of the energies of the different spin states relative to each other are observed with TZV and TZV+. This is due to the fact that the used geometries are *not* optimized for TZV und TZV+. [c] Spin-forbidden reaction. [d] Solv: including a solvent sphere in the calculation using the polarized continuum model (PCM) and acetonitrile as solvent; entropy ($T = 298$ K) and zero point correction energy (ZPCE) were calculated using the LanL2DZ basis set.

Introduction). This is in agreement with the electronic structure of **1** having a strong Fe−O and weak O−O bond which activates this intermediate for O−O bond homolysis. To explore the thermodynamics of this reaction, DFT calculations (B3LYP) have been performed on the homolytic cleavage of the O−O bond. The spectroscopic studies together with the calculations have shown that model **1̃** more closely resembles the properties of **1** (vide supra).[102] Therefore, it is likely that **1** has a water as the sixth ligand. Experimentally, the pK_A value of **1** is not known. Other Fe(III) complexes have pK_A values of 2 to 6 in aqueous solution (see, for example, refs 103 and 104). The fact that acetonitrile (even when small amounts of water are present) is not as good a solvent for the proton is consistent with the model that **1** has a water molecule bound. However, the Fe(IV)═O species produced in the homolysis reaction can be expected to be much more acidic.

To estimate the pK_A change upon oxidation of iron from +III to +IV on homolysis of the O−O bond, the relative pK_A values of **1̃** and the corresponding Fe(IV)═O intermediates have been calculated. The structures of the possible products $[Fe(NH_3)_4(OH_2)(O)]^{2+}$ (in total spin states $S = 1$, 2; from **1̃**) and $[Fe(NH_3)_4(OH)(O)]^{+}$ (**2̃**) ($S = 1$, 2; from **1̃a**) have been fully optimized using B3LYP/LanL2DZ and total energies have been obtained. Theoretical pK_A values have been determined corresponding to the reactions:

$$[Fe{-}OH_2]^{2+} + (H_2O)_n \rightarrow [Fe{-}OH]^{+} + [H(H_2O)_n]^{+};\ \Delta G \quad (6)$$

This is achieved by formally dividing this reaction into several steps and summing up their free energies. The first step is the deprotonation of the acid in the gas phase:

$$[Fe{-}OH_2]^{2+} \rightarrow [Fe{-}OH]^{+} + H^{+};\quad \Delta G_{GAS} \approx \Delta E_{GAS} - T{\cdot}\Delta S;\ T = 298\ \text{K}$$

The other steps describe the free solvation energies of the species involved:

$$[Fe{-}OH_2]^{2+} \rightarrow [Fe{-}OH_2]^{2+}(solv);\quad \Delta G_{SOLV}(Fe{-}OH_2) \approx \Delta E_{SOLV}(Fe{-}OH_2)$$

$$[Fe{-}OH]^{+} \rightarrow [Fe{-}OH]^{+}(solv);\quad \Delta G_{SOLV}(Fe{-}OH) \approx \Delta E_{SOLV}(Fe{-}OH)$$

Here, the solvation energies in acetonitrile are used (calculated with the PCM model[78]) neglecting the entropy contributions which can be expected to be one order of magnitude smaller for these charged ions. For the proton, a theoretical value of $\Delta G_{SOLV}(H^+) = -262.23$ kcal/mol ($T = 298$ K) is used which has been determined by large scale ab initio calculations on small water clusters $(H_2O)_n$.[105] With these numbers, the free energy of reaction 6 can be determined:

$$\Delta G \approx \Delta G_{GAS} + \Delta G_{SOLV}(Fe{-}OH) + \Delta G_{SOLV}(H^+) - \Delta G_{SOLV}(Fe{-}OH_2) \quad (7)$$

and the pK_A is defined:

$$pK_A = \frac{1}{2.30RT}\Delta G$$

Using the results from the B3LYP/LanL2DZ calculations (the larger TZV basis set (applied on the LanL2DZ structures) leads to similar results), the pK_A value of **1̃** is calculated to be 12.9 whereas for the $[Fe(NH_3)_4(OH_2)(O)]^{2+}$ systems, values of 8.0 ($S = 1$) and 6.9 ($S = 2$) are obtained. Although the absolute magnitude of the calculated pK_A values is unreliable in these types of calculations,[106] it is noteable that the Fe(IV)═O species are more acidic than **1̃** by 5 to 6 orders of magnitude. Note that this ΔpK_A value is independent of the applied value of $\Delta G_{SOLV}(H^+)$. Assuming that the pK_A value of **1** is in the range of 2 to 6, it is likely that an $[Fe(OH_2)(O)]$ intermediate species gets deprotonated during its formation under reaction conditions. To avoid complications due to the deprotonation reaction, the complete energetics of the homolytic O−O bond cleavage have been calculated for **1̃a** where no change occurs along the reaction pathway.

Table 9 shows the results obtained for **1̃a**. The homolysis of the O−O bond is endothermic in the calculations with the LanL2DZ basis set by ~30 kcal/mol for $S = 1$ and 2. The $S = 0$ spin state of the Fe(IV)═O complex is energetically very unfavorable by an additional +26 kcal/mol (9200 cm^{-1}) in all the different calculations and therefore, can be excluded from further consideration. The reaction energies are lowered by about 25% when solvation of the different species is included using the PCM model and acetonitrile as solvent. This is important

(102) Model **1̃** has an overly covalent π bond which is not unusual for transition metal electronic structure calculations. Since the Fe(IV)═O intermediate is treated at the same level of theory, this effect can be expected to cancel in the reaction energy calculations.

(103) Huheey *Inorganic Chemistry*; Harper & Row: Publishers: New York, 1972.

(104) La, T.; Miskelly, G. M. *J. Am. Chem. Soc.* **1995**, *117*, 3613−3614.

(105) Tawa, G. J.; Topol, I. A.; Burt, S. K.; Caldwell, R. A.; Rashin, A. A. *J. Chem. Phys.* **1998**, *109*, 4852−4863.

(106) Li, J.; Fisher, C. L.; Chen, J. L.; Bashford, D.; Noodleman, L. *Inorg. Chem.* **1996**, *35*, 4694−4702.

and shows that the solvent contributes to the reaction. Using a larger triple-ζ valence basis set (TZV) for the energy calculations (on the LanL2DZ structures) and including solvation, the reaction energies drop further to about +16 kcal/mol. Table 9 also contains the reaction energies calculated with TZV adding diffuse functions (TZV+; on the LanL2DZ geometries) and including the solvent effect. A small further decrease of 1 kcal/mol is obtained for the reaction energies compared to the TZV calculation. Therefore, the homolytic cleavage of the O−O bond in **1** is endothermic by about 15 kcal/mol. However, this unfavorable value is fully compensated by the entropy gain (about −14 kcal/mol at 298 K) and the zero-point energy correction (about −3 kcal/mol) as shown in Table 9. Summing up these different contributions, the homolytic cleavage is a thermoneutral reaction in terms of free energy driven by the entropy gain upon splitting of the O−O bond.

Only small changes of the reaction energy of the O−O bond homolysis occur when water is used as the sixth ligand of **1** instead of hydroxide (starting from $\tilde{\mathbf{1}}$) and the proton is kept bound to the Fe(IV)═O product. The calculation with the LanL2DZ basis set including solvation is endothermic by ∼30 kcal/mol for the $S = 1$, 2 spin states,[107] and with TZV (on the LanL2DZ geometries) the reaction energies are lowered to +23 kcal/mol (cf. Table 9). Since the energies obtained for O−O homolysis of $\tilde{\mathbf{1}}$ are comparable to those for $\tilde{\mathbf{1}}$**a**, the free energies can be expected to be very similar for both systems. Taking into account deprotonation of the Fe(IV)═O species, the actual homolytic cleavage reaction becomes:

$$[Fe(OH_2)(OOR)]^{2+}\ (\tilde{\mathbf{1}}) \rightarrow [Fe(OH)(O)]^{+}\ (\tilde{\mathbf{2}}) + {\cdot}OR + H^{+};\ \Delta E^{HC}$$

Here, ΔE^{HC} corresponds to the energy of the O−O bond homolysis of $\tilde{\mathbf{1}}$ as given in Table 9 plus the energy that would derive from the deprotonation of $\tilde{\mathbf{2}}$ according to eq 6. In a neutral solution, this latter energy can be estimated from the pK_A value. With the calculated pK_A of about 7 for the Fe(IV)═O species, this would add about +10 kcal/mol to the reaction energies given in Table 9. However, since the calculated pK_A values are too large compared to known experimental values (vide supra), the additional energy due to the deprotonation can be expected to be much lower. For a pK_A < 0 where deprotonation would be highly favorable, this energy would be negative and contribute to the driving force of the reaction.

In summary, the O−O homolysis is approximately a thermoneutral reaction in terms of free energy driven by the entropy gain upon breaking of the O−O bond. Importantly, the reaction energy is surprisingly low at +15 to 20 kcal/mol. Therefore, the highly oxidized Fe(IV) ion is strongly stabilized in the Fe(IV)═O complex as analyzed below.

B.4. Electronic Structure of the Fe(IV)═O Intermediate. Figure 8 shows the optimized geometry (B3LYP/LanL2DZ) of $[Fe(NH_3)_4(OH)(O)]^+$ ($\tilde{\mathbf{2}}$) ($S = 1$). The $S = 1$ ground state has a very short Fe−O bond (1.648 Å) corresponding to a large Fe−O force constant (5.7 mdyn/Å, $\tilde{\nu} = 902$ cm^{-1}; cf. Table 10). The calculated Fe−O bond length, stretching frequency, and force constant are in good agreement with experimental data determined for Fe−porphyrin systems with $S = 1$ on Fe(IV). The Fe−O distance for horseradish peroxidase compounds I and II has been estimated to be 1.64 Å from EXAFS spectroscopy.[23] A crystal structure of Cytochrome P450cam

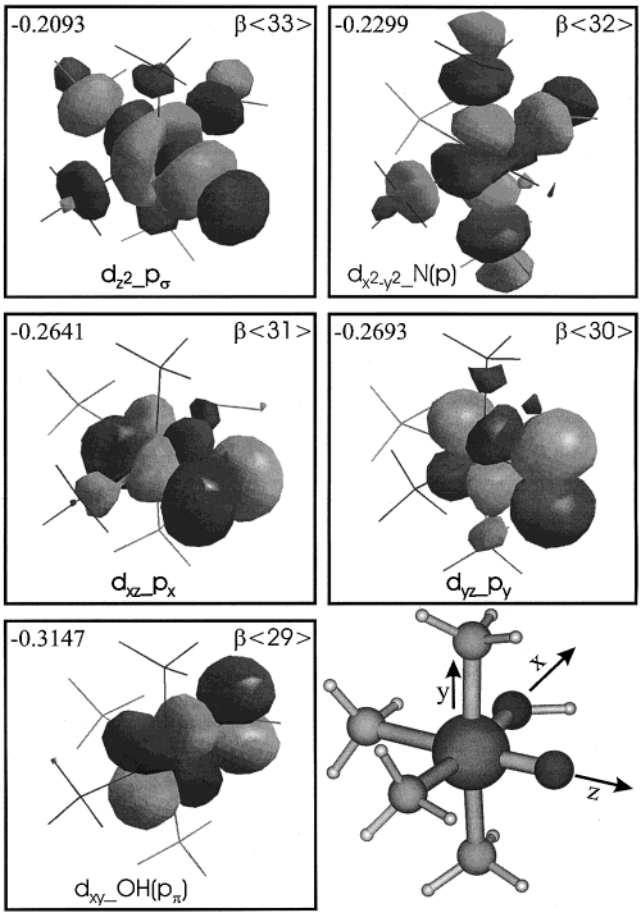

Figure 8. Contour plots of the molecular orbitals of $\tilde{\mathbf{2}}$ ($S = 1$) (cf. Figure 9 and Table 11) showing the interaction of the five d functions of iron(IV) with ligand donor orbitals. Bottom right: Optimized structure (B3LYP/LanL2DZ) of model system $\tilde{\mathbf{2}}$ ($S = 1$) which results from homolytic cleavage of the O−O bond in $\tilde{\mathbf{1}}$**a**. The coordinates of $\tilde{\mathbf{2}}$ are given in the Supporting Information, Table 6. Important structural parameters (in Å): Δ(Fe−O) = 1.648; Δ(Fe−OH) = 1.900.

compound I shows an Fe−O bond length of 1.65 Å.[19] For (TPP)Fe^{IV}═O, which contains a five-coordinate iron(IV) with $S = 1$, the Fe−O stretching frequency is found at 853 cm^{-1} corresponding to an Fe−O force constant of 5.32 mdyn/Å.[24,25] For a non-heme binuclear Fe(III)−O−Fe(IV)═O model complex, ν(Fe═O) is located at 840 cm^{-1}.[108] Although the iron is formally in the oxidation state +4 in $\tilde{\mathbf{2}}$, a comparison with Table 6 shows that the Mulliken charges on the metal are about the same as those in $\tilde{\mathbf{1}}$ and $\tilde{\mathbf{1}}$**a**, which are formally +3. In the following, the electronic structure of the Fe(IV)═O intermediate $\tilde{\mathbf{2}}$ will be analyzed for the $S = 1$ ground state. On the basis of this, the properties of the $S = 2$ and 0 states of $\tilde{\mathbf{2}}$ will be evaluated.

Figure 9 shows the MO diagram of $\tilde{\mathbf{2}}$ ($S = 1$) calculated with the B88P86 functional and a Slater-type triple-ζ (valence) basis set (see Experimental Section). Iron(IV) in the $S = 1$ state has a $[t_{2g}]^4$ electron configuration where two of the t_{2g} orbitals are singly occupied and one is doubly occupied. Therefore, only β d orbitals contribute to π bonding whereas α and β d functions form σ bonds with the ligands since the e_g orbitals are empty. This situation is analogous to $\tilde{\mathbf{1}}$ (vide supra) and the discussion of the MO diagram focuses on the β-spin orbitals. Since the oxo group is a very strong π donor using its p_x and p_y functions (in a coordinate system with the Fe═O bond along the z axis, cf. Figure 8), the two singly occupied t_{2g} functions are directed

(107) Note that the solvation energy is much larger for the complexes with the water ligand. This is due to the fact that these systems have a total charge of +2 compared to +1 for the deprotonated systems.

(108) Zheng, H.; Yoo, S. J.; Münck, E.; Que, L., Jr. *J. Am. Chem. Soc.* **2000**, *122*, 3789−3790.

Table 10. Calculated (B3LYP/LanL2DZ) Geometries and Properties of $[Fe(NH_3)_4(OH)(O)]^+$ ($\tilde{\mathbf{2}}$) with $S = 0$, 1, 2 (coordinates are given in the Supporting Information, Table 6)

	geometric parameters [a]						Mulliken charges			spin densities		
molecule	r(Fe−O)	r(Fe−OH)	r(Fe−N)[b]	ν(FeO)	k(FeO)	k(Fe−OH)[c]	Fe	O	O(H) [d]	Fe	O	O(H)[d]
$[Fe(NH_3)_4(OH)(O)]^+$, $S = 0$	1.664	1.834	2.079	878	5.347	2.943	+0.40	−0.38	−0.66			
$[Fe(NH_3)_4(OH)(O)]^+$, $S = 1$	1.648	1.900	2.073	902	5.699	2.558	+0.38	−0.33	−0.71	+1.21	+0.87	−0.05
$[Fe(NH_3)_4(OH)(O)]^+$, $S = 2$	1.650	1.850	2.212	895	5.640	2.774	+0.58	−0.34	−0.68	+2.98	+0.70	+0.15

[a] Bond length in Å. [b] Averaged over the four Fe−N bond lengths. [c] The corresponding Fe−OH stretching frequencies are in the range of 550−580 cm^{-1}. [d] Charge and spin density on the oxygen of the hydroxo ligand.

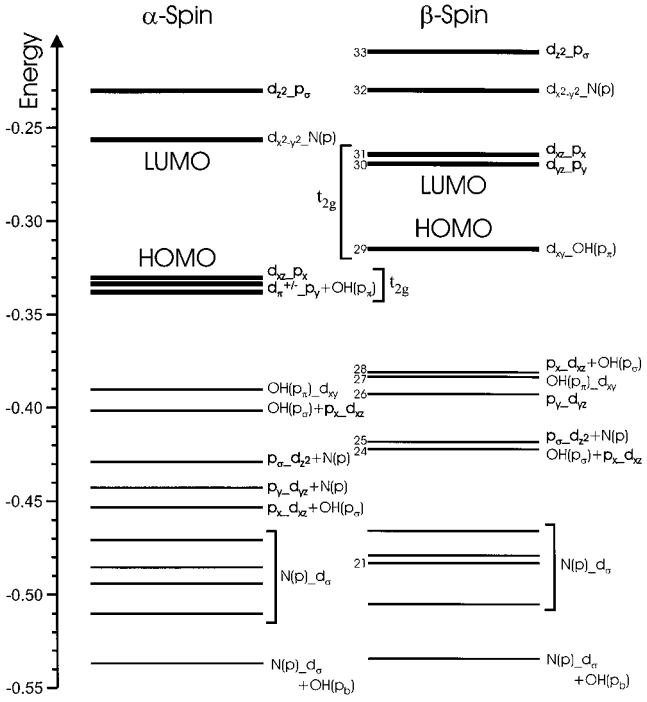

Figure 9. Molecular orbital diagram of $\tilde{\mathbf{2}}$ ($S = 1$) (the structure is given in Figure 8 together with the coordinate system) calculated with the B88P86/triple-ζ basis. The labels p_x, p_y, and p_σ refer to the donor functions of the oxo group with p_σ pointing along the Fe=O bond. The p donors on the oxygen of the hydroxo ligand are designated as $OH(p_\sigma)$ (within the Fe−O−H plane) and $OH(p_\pi)$ (perpendicular to the Fe−O−H plane), which give rise to a σ and π interaction with the d orbitals of iron(IV), respectively. The third p function of the hydroxo ligand is O−H bonding and at very low energy and is labeled $OH(p_b)$. For β-spin-orbitals included in Table 11, the continuous MO numbers (as they appear in the calculation) are given on the left side of the horizontal lines. Thick lines correspond to MOs with large iron d contributions (>50%).

toward the oxo ligand. The bonding combination of p_y with d_{yz}, p_y—d_{yz} ($\beta\langle 26\rangle$), has 40% metal and 49% oxo character as given in Table 11. The second π bonding MO, p_x—d_{xz} ($\beta\langle 28\rangle/\beta\langle 24\rangle$), is split by interaction with the $OH(p_\sigma)$ orbital, which is the σ donor function of the hydroxo ligand within the Fe−O−H plane, and has about 40% metal contribution distributed over these two levels. Both π interactions between Fe(IV) and the oxo ligand correspond to very covalent bonds. This is also reflected in their corresponding antibonding combinations, d_{yz}—p_y ($\beta\langle 30\rangle$) and d_{xz}—p_x ($\beta\langle 31\rangle$), which comprise the LUMO of $\tilde{\mathbf{2}}$ (S = 1). Both have ~60% metal and ~40% oxo character (cf. Table 11 and Figure 8). The third t_{2g} orbital, the HOMO d_{xy}—$OH(p_\pi)$ ($\beta\langle 29\rangle$), is occupied, hence it has no net bonding. The p_z function of the oxo ligand undergoes a σ interaction with the d_{z^2} orbital of iron and is therefore labeled p_σ. The corresponding bonding combination is located at low energy and is mixed with other molecular orbitals. Major contributions to the σ bond are found

Table 11. Charge Contributions of Important β Orbitals of $\tilde{\mathbf{2}}$ ($S = 1$) Calculated with the B88P86/Triple-ζ Basis

		energy	Fe	O		O(H)[a]		ΣN
no.	label	(hartree)	d	s	p	s	p	s+p
$\beta\langle 33\rangle$	d_{z^2}—p_σ	−0.2093	53	0	21	0	5	11
$\beta\langle 32\rangle$	$d_{x^2-y^2}$—N(p)	−0.2299	66	0	1	0	7	20
$\beta\langle 31\rangle$	d_{xz}—p_x	−0.2641	59	0	35	0	0	1
$\beta\langle 30\rangle$	d_{yz}—p_y (LUMO)	−0.2693	56	0	38	0	1	1
$\beta\langle 29\rangle$	d_{xy}—$OH(p_\pi)$ (HOMO)	−0.3147	76	0	0	0	19	0
$\beta\langle 28\rangle$	p_x—d_{xz} + $OH(p_\sigma)$	−0.3803	27	0	36	1	27	4
$\beta\langle 27\rangle$	$OH(p_\pi)$—d_{xy}	−0.3833	20	0	1	0	67	5
$\beta\langle 26\rangle$	p_y—d_{yz}	−0.3926	40	0	49	0	1	4
$\beta\langle 25\rangle$	p_σ—d_{z^2} + N(p)	−0.4179	5	2	55	0	6	24
$\beta\langle 24\rangle$	$OH(p_\sigma)$ + p_x—d_{xz}	−0.4218	15	0	22	1	47	7
$\beta\langle 21\rangle$	$N(p)/p_\sigma$–d_σ	−0.4830	27	2	13	0	1	47

[a] Contribution from the oxygen atom of the hydroxo ligand.

in p_σ–d_{z^2} ($\beta\langle 25\rangle$) and $N(p)/p_\sigma$–d_σ ($\beta\langle 21\rangle$). A clearer description of the strength of this interaction is available from the antibonding counterpart, d_{z^2}—p_σ ($\beta\langle 33\rangle$; cf. Figure 8), which has 53% metal and 21% oxo character corresponding to a strong σ bond. Since the e_g orbitals are also unoccupied for α-spin, there is a second contribution to this bond from the α orbitals which is of about the same magnitude. The remaining iron d orbital, $d_{x^2-y^2}$, forms a σ bond with the NH_3 and OH donors giving rise to $d_{x^2-y^2}$—N(p) ($\beta\langle 32\rangle$) which is shown in Figure 8.

In summary, the Fe(IV)=O bond is very covalent with one strong σ and two strong π interactions (note that the π bonds only count half because in this case only β orbitals contribute to bonding). This corresponds to a large amount of charge transfer from the oxo ligand to iron(IV) due to covalency and leads to a charge on the iron in $\tilde{\mathbf{2}}$ which is similar to that in the Fe(III) complexes $\tilde{\mathbf{1}}$ and $\tilde{\mathbf{1a}}$ (cf. Mulliken charges in Tables 6 and 10 and NPA and Voronoi charges in the Supporting Information, Table 7).[109] There is experimental evidence, however, that the covalency is somewhat overestimated in $\tilde{\mathbf{2}}$ (see Discussion). The large stabilization of the iron(IV) by the oxo group lowers the reaction energy of the O−O bond homolysis. In the case of the $S = 1$ ground state, the spin polarization is not very pronounced such that the σ interactions are similar for α- and β-spin. Hence, the calculated spin density on the oxo ligand is a direct measure for the π covalency as in the case of $\tilde{\mathbf{1}}$. In comparison, the π interaction in $\tilde{\mathbf{2}}$ is distinctly stronger with a spin density (taken from the B3LYP/LanL2DZ calculations) of +0.87 on the oxo group (cf. Table 10) compared to +0.29 on the oxygens of the ^{t}BuOO$^-$ ligand (cf. Table 6) in $\tilde{\mathbf{1}}$.

The $S = 1$ ground state is followed by the $S = 2$ state which is only 700 cm^{-1} higher in energy (B3LYP/LanL2DZ). The optimized structure of $\tilde{\mathbf{2}}$ ($S = 2$) has a very short Fe−O bond

(109) The Voronoi charge analysis is electron density based and, hence, more useful here relative to the orbital based Mulliken analysis. Using the Voronoi analysis as implemented in ADF, the calculated change of the charge on iron when going from Fe(II) to Fe(III) in a simple hexaqua model complex is about +0.4. This is about twice as large as the change between Fe(III)−OO^{t}Bu and Fe(IV)=O (cf. Supporting Information, Table 7).

corresponding to a large Fe−O force constant (cf. Table 10) indicating that the Fe−O bond is comparable to the $S = 1$ case. The $S = 2$ spin state has a $[t_{2g}]^3[e_g]^1$ electron configuration where all three t_{2g} orbitals are singly occupied. The fourth electron occupies one of the e_g functions. Due to the strong σ interaction between iron(IV) and the oxo ligand, the d_{z^2} orbital is raised in energy compared to $d_{x^2-y^2}$, hence the latter orbital becomes occupied in the $S = 2$ case. In Figure 9, the splitting of the e_g orbitals is about 4500 cm^{-1}. Importantly, *the $d_{x^2-y^2}$ function does not interact with the oxo ligand, but the energetic position of this orbital determines the spin state of* $\tilde{\mathbf{2}}$ ($S = 1$ or 2). Therefore, the spin of the ground state does not depend on the Fe(IV)−oxo group, but on the donor properties of the equatorial ligands to iron. This is reflected by the very similar properties of the Fe=O bond in the $S = 1$ and 2 case. In a weak ligand field, the $d_{x^2-y^2}$ orbital will be low in energy and the $S = 2$ state is energetically more favorable whereas a stronger ligand field favors $S = 1$. The applied NH_3/OH^- donor set in $\tilde{\mathbf{2}}$ creates a ligand field of intermediate strength, and correspondingly, both states ($S = 1$ and 2) are very close in energy.

The $S = 0$ state is strongly destabilized by 9200 cm^{-1} relative to the ground state ($S = 1$) which is due to the loss of exchange stabilization energy because of spin pairing and the reduced Fe(IV)=O bond strength which is reflected by a longer Fe−O bond and smaller Fe−O force constant. In the $S = 0$ spin state, which has a $[t_{2g}]^4$ electron configuration, two of the three t_{2g} orbitals are doubly occupied, hence they do not contribute to net bonding. Therefore, one of the π donor orbitals of the oxo group is oriented toward a fully occupied t_{2g} orbital which leads to lone-pair repulsion and hence a longer Fe=O bond.

Discussion

The resonance Raman spectrum of low-spin [Fe(TPA)-(OH_x)(OO^tBu)]$^{x+}$ (**1**) is assigned using isotope perturbation experiments. The O−O stretch is identified at 796 cm^{-1} and the Fe−O stretch is found at 696 cm^{-1}. An additional band at 490 cm^{-1} is assigned to a mixed O−C−C/C−C−C bending vibration of the *tert*-butyl group that gains resonance enhancement from a large admixture of the Fe−O stretch. Since the isotope perturbations in Figure 2 show that the vibrations of the Fe−O−O−$C(CH_3)_3$ unit are strongly mixed, the observed vibrational frequencies are not proper reflections of the corresponding bond strengths. These can only be determined in the form of vibrational force constants from a normal coordinate analysis (NCA). However, since only three normal modes have been found experimentally, the matrix of force constants for the NCA is highly underdetermined. To address this problem, an initial force field has been obtained from density functional theory and selected force constants have been fitted to the experimental data following the QCA-NCA scheme.[64] Using this procedure, the force constants have been determined to be 2.92 mdyn/Å (O−O) and 3.53 mdyn/Å (Fe−O). These show that **1** has a very strong Fe−O and weak O−O bond. To understand the electronic structure that leads to the observed bond strengths, several spectroscopies and DFT calculations have been applied to probe the Fe(III)−alkylperoxo bond in **1**.

Electronic structure calculations on **1** show the presence of a π bond between the π_v^* orbital of the $^tBuOO^-$ ligand (HOMO) and a t_{2g} orbital of iron. This π bond gives rise to a moderately intense CT transition around 600 nm, which is probed by absorption, MCD, and resonance Raman spectroscopies. Both the Fe−O (696 cm^{-1}) and O−O (796 cm^{-1}) stretches are resonance enhanced with respect to this broad 600 nm absorption band, which corresponds to a pseudo-**A** signal in the MCD spectrum. Analysis of the spectroscopic data shows that there are two intense transitions hidden under the broad envelope of the 600 nm band that correspond to the two components of the pseudo-**A** signal. These two excited states are displaced along the Fe−O and O−O bonds relative to the ground state, hence both are of CT type. On the other hand, the DFT calculations clearly show that there is only one intense CT transition in the visible region of the absorption spectrum. Therefore, the CT state corresponding to the π bond is mixed with a ligand field state by Configuration Interaction (CI), giving rise to two excited states with significant CT character in agreement with the analysis of the pseudo-**A** MCD signal. The integral sum of the intensities of the two corresponding absorption bands can then be used to calculate the relative donor strength of this π bond between the alkylperoxo ligand and Fe(III). In comparison with a related alkylperoxo complex of Cu(II) (cf. Table 5), the relative donor strength of the π bond is relatively weak in **1**, which is inconsistent with the large Fe−O force constant determined from vibrational spectroscopy. Since the force constant probes the total bonding between the metal and the alkylperoxo ligand, there must be bonding contributions in addition to the π bond in **1** that lead to the large Fe−O force constant. With the help of the DFT calculations, these additional contributions to the Fe−O bond arise from the σ interactions between the π_h^*, π_h^b, and σ^b orbitals of the alkylperoxo ligand and an e_g function of Fe(III). Importantly, the σ interaction from the O−O bonding orbitals π_h^b and σ^b dominates, which is in agreement with the observed trend in force constants: whereas exclusive donation from O−O antibonding π^* orbitals should lead to a strong Fe−O and O−O bond, the σ interaction from O−O bonding orbitals leads to a strengthening of the Fe−O and weakening of the O−O bond. This leads to the low experimental O−O force constant of 2.92 mdyn/Å. The DFT calculations overestimate the covalency of the π bond and seem to underestimate the strength of the σ interaction, hence the experimental force constants are not accurately reproduced (cf. Table 7).

The experimentally probed electronic structure of **1** gives insight into the observed reactivity of this complex: the strong Fe−O and weak O−O bond represent a step in the direction of the experimentally observed homolytic cleavage of the O−O bond. With the help of DFT calculations, the thermodynamics of this reaction are evaluated in detail. The homolytic cleavage of the O−O bond is endothermic by about 15−20 kcal/mol. This number includes solvent effects which are important for this reaction because they strongly stabilize the products. The endothermicity is compensated by the entropy contribution at room temperature (about −14 kcal/mol) and the zero-point correction energy (about −3 kcal/mol). Therefore, the reaction is overall thermoneutral in terms of free energy and entropy driven.

It is remarkable that the homolytic cleavage of the O−O bond is only endothermic by 15 to 20 kcal/mol. This means that the Fe(IV)=O bonding must greatly stabilize the formal oxidation state +IV of iron. This is achieved by a very covalent Fe=O bond as shown in Scheme 4, left. The three p functions of the oxo group form two very covalent π bonds with the d_{xz} and d_{yz} orbitals of iron (in an orientation with the Fe=O bond along the *z* axis) and a σ bond with d_{z^2}. The calculated Mulliken charge of iron in the Fe(IV)=O intermediate (Table 10) is close to that of the Fe(III)−alkylperoxo complex (Table 6), which indicates that there is little net oxidation of iron in the Fe(IV)=O species due to the strong donor ability of the oxo ligand (cf. also Supporting Information, Table 7). In fact, this bonding description is somewhat closer to Fe(III)−oxyl than

Scheme 4

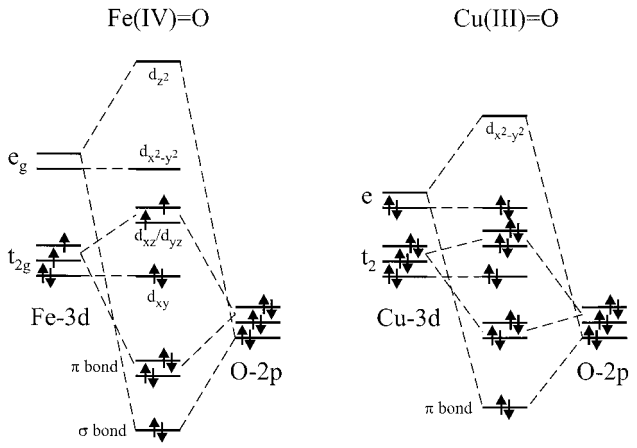

Fe(IV)−oxo. This can be experimentally probed by X-ray absorption (XAS) and Mössbauer spectroscopies. The energies of metal K-edge preedge transitions (corresponding to excitations of core 1s electrons to empty d orbitals) are sensitive probes for the oxidation state of the metal as they shift to higher energy by 1−1.4 eV per one-electron oxidation. This has been observed for iron, copper, and titanium.[110] For horseradish peroxidase, K-edge preedge spectra have been recorded for the Fe(III) form of the enzyme and compounds I and II which contain Fe(IV)═O ($S = 1$).[22] The observed shift of the preedge feature in going from +3 to +4 is about +0.5 eV or less, which is consistent with the Fe(III)−oxyl description. Alternatively, Mössbauer spectra of these species show a decrease of the isomer shift of about 0.20 to 0.25 mm/s when going from the ferric to the ferryl(+4) species,[20,21] which is closer to the Fe(IV)−oxo description. In summary, the experimental evidence together with the calculations presented here indicate that the Fe(IV)═O unit is highly covalent with significant Fe(III)−oxyl character, but further experiments are needed to quantify this bond which appears to be overly covalent in the DFT calculations. The electronic structure of the Fe(IV)═O ($S = 1$) unit in corresponding heme systems[111] has similarities to the description obtained here for non-heme environments. Similar atomic charges and spin-densities are obtained, which indicates that the covalency of the Fe(IV)═O bond is similar.

The Fe(IV)═O intermediate can exist in two spin states ($S = 1$, 2) and their relative energies depend on the ligand environment of iron. With ligands of intermediate donor strengths, both spin states $S = 1$ (electron configuration: $(d_{xy})^2(d_{xz})^1(d_{yz})^1$; cf. Scheme 4) and $S = 2$ (electron configuration: $(d_{xy})^1(d_{xz})^1(d_{yz})^1(d_{x^2-y^2})^1$) of the Fe(IV)═O intermediate are close in energy. This is due to the fact that the energy of the $d_{x^2-y^2}$ orbital, which gets occupied in the $S = 2$ case, does not depend on the Fe(IV)−oxo interaction but rather on the equatorial ligand field that determines the ground state. Thus, the Fe−O bond has similar properties in the $S = 1$ and 2 spin states (cf. Table 10). In contrast, the $S = 0$ spin state where two t_{2g} orbitals are doubly occupied has a distinctly weaker Fe(IV)═O bond and is energetically unfavorable.

An even weaker metal═O bond is expected for the putative Cu(III)═O intermediate that would arise from homolytic cleavage of the O−O bond in the related four-coordinate Cu(II)−alkylperoxo complexes. This is reflected by the observation that these systems undergo different reactions.[94] Scheme 4 shows the basic MO diagram for such a Cu(III)═O species in comparison to Fe(IV)═O. In the copper case, the combination of the trigonally distorted tetrahedral ligand field and one strongly π bonding ligand leads to an electronic structure where the $d_{x^2-y^2}$ orbital (quantization along the trigonal axis) is highest in energy. This is very similar to the electronic structure of blue copper proteins.[112] The unoccupied $d_{x^2-y^2}$ orbital of the Cu(III) species forms a π bond with the oxo ligand,[113] and therefore no change to the metal−oxo π interaction occurs (π bond order = 1) compared to Fe(IV). In fact, a stronger π interaction can be expected for Cu(III) since the d manifold of Cu is lower in energy by about 0.6 eV (determined for Cu(II) vs Fe(III); see ref 114). Correspondingly, the Cu(III)═O intermediate has been described as a Cu(II)−oxyl species based on DFT calculations.[94] On the other hand, the σ bond that is present in the Fe(IV)═O intermediate is eliminated in the case of Cu(III)═O. This leads to a loss of charge donation from the oxo ligand to Cu(III) and a weaker metal═O bond[115] and, correspondingly, to a large energetic destabilization of the Cu(III)═O species. Therefore, the homolytic cleavage reaction of the O−O bond will be much more endothermic for Cu(II)−alkylperoxo complexes compared to Fe(III). In the case of Cu, the favorable entropy term would not compensate this endothermicity and the homolytic cleavage of the O−O bond is overall energetically unfavorable.

Acknowledgment. This work was supported by the National Instituts of Health (GM-40392 to E.I.S. and GM-33162 to L.Q.). N.L. thanks the Deutscher Akademischer Austauschdienst (DAAD) for a postdoctoral fellowship. Mr. Peng Chen is acknowledged for making unpublished results on the Cu(III)═O intermediate available for comparison with Fe(IV)═O.

Appendix

In the **B** matrix, an angle bending coordinate is defined as a displacement along the vectors $\vec{v}_A$ and $\vec{v}_B$ at the terminal atoms perpendicular to the bond (of length $1/|\vec{r}|$ with $|\vec{r}|$ being the corresponding bond distance) and along $\vec{v}_C$ at the central atom.[116] Hence, distortions along bends given in angstroms do not provide useful information. To estimate the actual distortion in

(110) (a) Westre, T. E.; Kennepohl, P.; DeWitt, J. G.; Hedman, B.; Hodgson, K. O.; Solomon, E. I. *J. Am. Chem. Soc.* **1997**, *119*, 6297−6314. (b) DuBois, J. L.; Mukherjee, P.; Stack, T. D. P.; Hedman, B.; Solomon, E. I.; Hodgson, K. O. *J. Am. Chem. Soc.* **2000**, *122*, 5775−5787. (c) Brant, P.; Stevens, P. A.; Solomon, E. I. Manuscript in preparation.

(111) Kuramochi, H.; Noodleman, L.; Case, D. A. *J. Am. Chem. Soc.* **1997**, *119*, 11442−11451.

(112) (a) Randall, D. W.; Gamelin, D. R.; LaCroix, L. B.; Solomon, E. I. *JBIC* **2000**, *5*, 16−29. (b) Solomon, E. I.; Randall, D. W.; Glaser, T. *Coord. Chem. Rev.* **2000**, *200−202*, 595−632.

(113) Chen, P.; Solomon, E. I. Unpublished data.

(114) Shadle, S. E. *Ligand K-Edge X-ray Absorption Spectroscopic Studies of the Electronic Structure of Inorganic Model Complexes and Metalloprotein Active Sites*; Stanford University: Stanford, CA, 1994.

(115) This is reflected by the shortening Δr of the metal−O bond when going from [metal−alkylperoxo] to $[metal{=}O]^+$ upon homolytic cleavage of the O−O bond. In the case of Cu(II/III) a $\Delta r = 0.11$ Å results (calculated in ref 94) whereas for Fe(III/IV), a larger value of $\Delta r = 0.17$ Å is obtained (cf. Tables 6 and 10).

(116) Wilson, E. B., Jr.; Decius, J. C.; Cross, P. C. *Molecular Vibrations*; Dover Publications: New York, 1980.

(117) Pate, J. E.; Cruse, R. W.; Karlin, K. D.; Solomon, E. I. *J. Am. Chem. Soc.* **1987**, *109*, 2624.

(118) Baldwin, M. J.; Ross, P. K.; Pate, J. E.; Tyeklar, Z.; Karlin, K. D.; Solomon, E. I. *J. Am. Chem. Soc.* **1991**, *113*, 8671.

(119) Neese, F.; Solomon, E. I. *J. Am. Chem. Soc.* **1998**, *120*, 12829−12848.

(120) Redington, R. L.; Olson, W. B.; Cross, P. C. *J. Chem. Phys.* **1962**, *36*, 1311−1326.

(121) Oakes, J. M.; Harding, L. B.; Ellison, G. B. *J. Chem. Phys.* **1985**, *83*, 5400−5406.

(122) Ory, H. A. *Anal. Chem.* **1960**, *32*, 509−511.

(123) Butwill Bell, M. E.; Laane, J. *Spectrochim. Acta* **1972**, *28A*, 2239−2245.

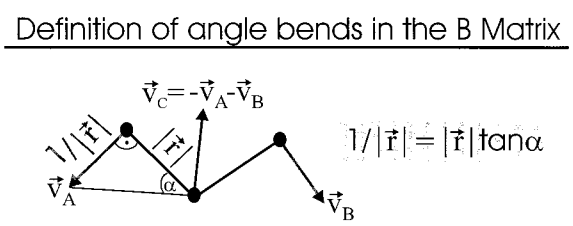

grad, the effective displacement along $|\vec{v}_A|$ and $|\vec{v}_B|$ for a unit displacement of the corresponding normal coordinate has to be calculated. This information can be obtained from the atomic displacement matrix **A**, which is calculated by:[116]

$$\mathbf{A} = M^{-1}\mathbf{BFL}\Lambda^{-1} \qquad \text{(A1)}$$

with $M^{-1}\mathbf{B}$ being the mass-weigthed **B** matrix; **F** is the matrix of force constants, **L** is a matrix that consists of the eigenvectors from NCA, and the Λ^{-1} is a unit matrix with the reciprocal of the eigenvalues as the diagonal elements. Here, an approximate version of eq A1 was applied using only the column of the **B** matrix defining the respective bending coordinate and only their diagonal force constant. This gives a rough estimate of the vectors $\vec{v}_A$, $\vec{v}_B$ and $\vec{v}_C$. Projecting $\vec{v}_C$ on $\vec{v}_A$ and $\vec{v}_B$ leads to $\vec{v}'_A$ and $\vec{v}'_B$ which are no longer perpendicular to the corresponding A−C and B−C bonds. Using eq 5, the absolute displacement along $\vec{v}'_A$ and $\vec{v}'_B$ is calculated and the distortion in grad is estimated with the equation:

$$|\vec{v}'| = |\vec{r}| \cdot \tan\alpha$$

which is only strictly valid if $\vec{v}'$ is orthogonal to $\vec{r}$, but the small deviation is neglected here. Even if the applied approximations (especially to eq A1) are rough, the calculated values should not be off by more than 1 grad.

Supporting Information Available: Figures of the fully optimized structures of low-spin $[Fe(NH_3)_4(OH)(OO^tBu)]^+$ (**1̃a**) and low-spin $[Fe(Ime)_3(NH_3)(OH_2)(OO^tBu)]^{2+}$, Cartesian coordinates of the optimized structures of all three Fe(III)−OO^tBu model systems, complete force field of **1̃** used for NCA, Cartesian coordinates of the optimized structures of $[Fe(NH_3)_4(OH)(O)]^+$ (**2̃**) for $S = 0-2$, and NPA and Voronoi charges for **1̃**, **1̃a**, and **2̃** ($S = 1, 2$) (PDF). This material is available free of charge via the Internet at http://pubs.acs.org.

JA010165N